

MoS₂/MX₂/MoS₂ TRILAYER TMDC FIELD EFFECT TRANSISTOR BASED POTENTIOMETRIC NANOBIOSENSORS

A thesis submitted in partial fulfillment of the requirements for the degree of
Master of Science in Electrical and Electronic Engineering

by

Abir Shadman

Student No: 1014062220 P



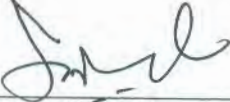
Department of Electrical and Electronic Engineering
Bangladesh University of Engineering and Technology

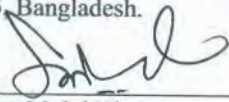
August 2016


Approval

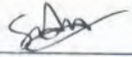
The thesis titled “**MoS₂/MX₂/MoS₂ TRILAYER TMDC FIELD EFFECT TRANSISTOR BASED POTENTIOMETRIC NANOBIOSENSORS**” submitted by Abir Shadman, Student No: 1014062220 P, Session: October 2014, has been accepted as satisfactory in partial fulfillment of the requirements for the degree of Master of Science in Electrical and Electronic Engineering on August 20, 2016.

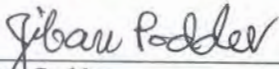
Board of Examiners

1. 

Dr. Quazi Deen Mohd Khosru
Professor
Department of Electrical and Electronic Engineering
Bangladesh University of Engineering and Technology
Dhaka – 1205, Bangladesh. Chairman
(Supervisor)
2. 

Dr. Quazi Deen Mohd Khosru
Professor and Head
Department of Electrical and Electronic Engineering
Bangladesh University of Engineering and Technology
Dhaka – 1205, Bangladesh. Member
(Ex officio)
3. 

Dr. Mohammad Jahangir Alam
Professor
Department of Electrical and Electronic Engineering
Bangladesh University of Engineering and Technology
Dhaka – 1205, Bangladesh. Member
4. 

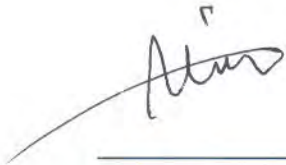
Dr. Shaikh Asif Mahmood
Associate Professor
Department of Electrical and Electronic Engineering
Bangladesh University of Engineering and Technology
Dhaka – 1205, Bangladesh. Member
5. 

Dr. Jibon Podder
Professor
Department of Physics
Bangladesh University of Engineering and Technology
Dhaka – 1000, Bangladesh. Member
(External)

Declaration

It is hereby declared that this thesis or any part of it has not been submitted elsewhere for the award of any degree or diploma.

Signature of the Candidate

A handwritten signature in black ink, appearing to read 'Abir', is written above a horizontal line. The signature is stylized with a long horizontal stroke extending to the left.

(Abir Shadman)

To my beloved parents

Acknowledgment

All praise goes to the Almighty for giving me the patience and drive required to complete my M.Sc. research and finish the dissertation in due time.

I would begin by heartily thanking my thesis supervisor Dr. Quazi Deen Mohd Khosru, Professor and Head, Department of Electrical and Electronic Engineering (EEE), Bangladesh University of Engineering and Technology (BUET), for his generous help, edifying suggestions and well-defined guidance throughout the thesis work. I feel grateful to him for giving me sufficient freedom and having faith in my capabilities, which made the research work very much enjoyable for me. His passion and dedication to academic research has motivated me to push my boundaries harder and excel at my research work, which I believe will inspire me to be a better researcher in future days to come.

I want to express my gratitude to Imtiaz Ahmed, Lecturer, Department of Electrical and Electronic Engineering (EEE), Bangladesh University of Engineering and Technology (BUET), for his kind help with the discussion on Junction Less FET. I also want to thank Kanak Datta, Lecturer from the same institution, for his sincere help with the DFT simulations.

I would like to thank my parents and dedicate my thesis to them. They have been the encouragement behind my every successful endeavor. This thesis work is not an exception and this would not have been completed without their constant support and inspiration.

Finally, I put forward my humble gratitude to all my colleagues, friends and well-wishers for their help, support and words of encouragement during my research work.

Abstract

The ability to detect biomolecules and chemicals accurately, effectively, and promptly in variety of environments including applications in homeland security, clinical diagnoses, environmental monitoring, food safety, etc. has always been an important issue. For each of these applications, it is highly desirable that a small, ultra-sensitive, versatile and robust sensor be created. During the last decade, enormous progress in the synthesis of 1-D nanostructured materials and nanoparticles has allowed the fabrication of nanometer-sized sensors. Such materials and devices, with large surface-to-volume ratios and Debye length comparable to their small size, have already displayed superior sensitivity for the detection of various chemical and biological species. Their extremely small-scale also enables the miniaturization of sensors (e.g., portable, handheld sensors) as well as their multiplexing functionality to achieve simultaneous detection of multiple target molecules in a given sample. In spite of huge existing research regarding the fabrication of nanoscale bio and chemical sensors, the understanding of their sensing mechanism has been limited. In this thesis, we develop a comprehensive theoretical framework to correlate the geometry and physical properties of nanoscale sensors to their sensing performance of target molecules. This framework provides guidance for approaches about the sensor design and optimization. This work focuses on detection scope of biomolecule both in wet and dry environment. Label free electrical detection of biomolecules like enzyme, cell, DNA etc. with state of the art device like the one Junctionless Double Gate MOSFET has been investigated with the help of an analytical model. The impact of neutral biomolecules on the electrical characteristics of n-type Junctionless Double Gate MOSFET has been analyzed under dry environment situation. Factors crucial to biosensor like biomolecule's position and their percentage area coverage have been investigated to find optimum arrangement of biomolecule for maximum sensitivity. In addition, this work also offers a comprehensive study of performance of sensor as a function of device physical parameters to maximize detection capability.

Table of Contents

Approval	i
Declaration	ii
Acknowledgment	iv
Abstract	v
Table of Contents	vi
List of Figures	viii
List of Abbreviations	xii
List of Symbols	xiii
1 Introduction	1
1.1 The Rationale of ‘Nano-scale’ Sensors.....	1
1.2 Mechanisms of Detection: Biosensors vs. Chemical Sensors	2
1.3 Technologies in Biosensing	3
1.3.1 Electronic Detection.....	3
1.3.2 Magnetic Detection	4
1.4 Next Generation Potentiometric Biosensor	5
1.4.1 Switching to 2D materials and heterostructures	5
1.5 Motivation for choosing trilayer TMDC for biosensor operation	7
1.6 Some Experimental Setups of TMDC Sensor	8
1.7 Dielectrically Modulated Junctionless FET.....	10
1.8 Thesis Objectives	11
1.9 Thesis Organization	11
2 Simulation Study of Electrical Response of Multilayer TMDC Nanobiosensor in Wet Environment	13
2.1 Electronic Properties of Trilayer Transition Metal Dichalcogenides	13
2.2 Model System	14
2.3 Model Equations	16
2.4 Simulator Validation.....	21
2.5 Current-Voltage modelling of TMDC FET (Drift-Diffusion Region)	21
2.6 Result and Discussion	22
2.6.1 Application as pH sensor	22
2.6.2 Application as Biosensor	28
3 Analytical Modeling of Dielectric Modulated Double Gate Junctionless MOSFET	31
3.1 Introduction.....	31
3.2 Device Structure.....	33
3.3 Working principle of the device	34
3.4 Analytical Model Development.....	34
3.5 Results and Discussions	40
3.5.1 Variation of Sensitivity with Position of Biomolecule	40

3.5.2	Dependence of Sensitivity on Biomolecule's Position when Region IV is connected to Drain	41
3.5.3	Dependence of Sensitivity on Position of Biomolecule when Region I is connected to drain	43
3.5.4	Summary	45
4	Analytical Modeling of TMDC DMFET	46
4.1	Device Structure.....	46
4.2	Differential System Establishment	46
4.3	Evaluating the Constants <i>C1, C2, C3 and C4</i>	49
4.4	Result and Discussion	50
4.5	DMFET Simulation using NEGF approach.....	52
4.5.1	Simulation approach:	52
4.6	Result and Discussion	53
5	Conclusion	55
5.1	Summary	55
5.2	Suggestions for Future Work	55
	References	57
	Appendix A	63
	Appendix B	66
	Appendix C	67

List of Figures

Figure 1.1 Comparative size of some key biological structures and nanomaterials[4].	2
Figure 1.2 A conceptual diagram of a biosensor composed of recognition module and transducer.....	3
Figure 1.3 Electronic detection scheme with SiNW biosensors. Introduction of target molecules causes a change in conductance across the nanowire. The conductance returns to its initial level after rinsing with buffers[11].....	4
Figure 1.4 ITRS roadmap[16] for transistor scaling in terms of physical channel length.	5
Figure 1.5 Intel’s innovation enabled technology pipeline info graphic.	6
Figure 1.6 MoS ₂ -based FET biosensor device. (a) Schematic diagram of MoS ₂ -based FET biosensor. For biosensing, the dielectric layer covering the MoS ₂ channel is functionalized with receptors for specifically capturing the target biomolecules. The charged biomolecules after being captured induce a gating effect, modulating the device current. An electrolyte gate in the form of a Ag/AgCl reference electrode is used for applying bias to the electrolyte. The source and drain contacts are covered with a dielectric layer to protect them from the electrolyte (not shown in this figure). (b) Optical image of a MoS ₂ flake on 270 nm SiO ₂ grown on degenerately doped Si substrate. Scale bar, 10 μm. (c) Optical image of the MoS ₂ FET biosensor device showing the extended electrodes made of Ti/Au. Scale bar, 10 μm. (d) Image and schematic diagram (inset figure) of the chip with the biosensor device and microfluidic channel for containing the electrolyte. Inlet and outlet pipe for transferring the fluid and the reference electrode are not shown in the figure(Courtesy [41]).	8
Figure 1.7 A MoS ₂ nanosheet biosensor and contact angles of different surfaces. (a) Schematic of a MoS ₂ biosensor configured as a PSA, detecting label free immunoassay, illustrating PSA antibody functionalized MoS ₂ surface (top) and subsequent binding of PSA antigen with antibody receptors. The MoS ₂ nanosheet biosensor consists of a gate insulator of SiO ₂ (300 nm) and a drain-source metal contact of Ti/Au (15nm/300 nm) (b) The water contact angle measurement to confirm hydrophobic characteristics of different substrates: the water contact angle of MoS ₂ , Au, and SiO ₂ substrate are 75.75, 75.72, and 23.1 degree, respectively. The contact angle of MoS ₂ surface, which is more	

hydrophobic than Si-based substrates, is comparable to that of Au surface. This suggests that MoS₂ nanosheet is an excellent candidate for functionalizing antibody and protein due to its hydrophobic surface. (Courtesy [44]) 9

Figure 1.8 Illustrations (a) and optical micrographs (b) of insulating-layer coated (left) and insulating-layer-free (right) MoS₂ FET biosensors [43]. 9

Figure 1.9 Flow chart for fabricating a MoS₂ transistor biosensor: (a) printing of a few-layer MoS₂ flake onto a substrate; (b) fabrication of Ti/Au D/S contacts; (c) ALD growth of the HfO₂ effective layer on top of the MoS₂ channel and coating of D/S contacts with thick SiO_x layers; (d) integration of a PDMS liquid reservoir on top of the MoS₂ transistor for measuring sensor responses from different TNF concentrations under thermodynamic equilibrium condition and determining the affinity of the antibody-(TNF- α) pair; (e) integration of a microfluidic inlet/outlet tubing kit driven by a motorized syringe pump on top of the transistor (f) functionalization of the HfO₂ effective layer with antibody receptors and subsequent TNF- α detection (Courtesy [45]). 10

Figure 2.1 MoS₂/MX₂/MoS₂ trilayer structure used in this study. 13

Figure 2.2 Simple Schematic representations of the pH sensor (left) and Biomolecule (Amino Acid) sensor (right) used in this paper. Here SiO₂ is used as top and bottom oxide for pH and biosensor. None of the devices shown in this figure is drawn to scale. 15

Figure 2.3 Our simulator is benchmarked with that of reported Si pH sensor[54]. Curves indicate the potential profiles associated fluid gate (linear regime, V_{BG} = 0V, V_{FG} = 1V) operation. 21

Figure 2.4 depicts the increase of the difference of V_T for various pH with the increase of bottom oxide thickness and provides insights towards the upward movement of the ΔV_T for various thicknesses. This figure is for MoS₂/WS₂/MoS₂ FET pH sensor. Here, V_{FG} = 1V. 23

Figure 2.5 Figure shows shift of V_T with pH for back gate operation, which is above the Nernst limit (MoS₂/WS₂/MoS₂ FET pH sensor). The linearity of the curves can be traced to the equation 2.15. 24

Figure 2.6 depicts the increase of the difference of V_T for various pH with the increase of bottom oxide thickness and provides insights towards the upward movement of the ΔV_T for various thicknesses. This figure is for MoS₂/MoSe₂/MoS₂ FET pH sensor. Here, V_{FG} = 1V. 24

Figure 2.7 Figure shows shift of V_T with pH for back gate operation, which is above the Nernst limit ($\text{MoS}_2/\text{MoSe}_2/\text{MoS}_2$ FET pH sensor). The linearity of the curves can be traced to the equation 2.15. 25

Figure 2.8 depicts the increase of the difference of V_T for various pH with the increase of bottom oxide thickness and provides insights towards the upward movement of the ΔV_T for various thicknesses. This figure is for $\text{MoS}_2/\text{WSe}_2/\text{MoS}_2$ pH sensor. Here, $V_{FG} = 1\text{V}$ 25

Figure 2.9 Figure shows shift of V_T with pH for back gate operation, which is above the Nernst limit ($\text{MoS}_2/\text{WSe}_2/\text{MoS}_2$ FET pH sensor). The linearity of the curves can be traced to the equation 2.15. 26

Figure 2.10 Sensitivity v/s Bottom oxide thickness for all these trilayer TMDC FET pH sensors. 26

Figure 2.11 shows the narrowing of drain current in the sub threshold region with the increase of top oxide thickness. This figure is for $\text{MoS}_2/\text{WSe}_2/\text{MoS}_2$ pH sensor. Here, $V_{FG} = 1\text{V}$ 27

Figure 2.12 depict the sensitivity of $\text{MoS}_2/\text{WSe}_2/\text{MoS}_2$ TMD FET pH sensor for top oxide scaling. 27

Figure 2.13 pH sensitivity for different bottom oxide thickness with top oxide thickness as a parameter for $\text{MoS}_2/\text{WSe}_2/\text{MoS}_2$ trilayer ISFET. Increasing top oxide thickness reduces sensitivity and we get opposite trend for bottom oxide. 28

Figure 2.14 I_d - V_{BG} characteristics of different-trilayer TMDC heterostructure biosensors for different no of Aspartic acids. Spread of the drain current in the subthreshold region is the lowest for $\text{MoS}_2/\text{WS}_2/\text{MoS}_2$ trilayer DGFET biosensor for various no. of Aspartic acids among these three FETs. For these three heterostructure FETs, no significant difference in device current is observed for various acids in ‘on’ region resulting in a low sensitivity for all of them in ‘on’ condition. Here, V_{FG} is considered 1V 29

Figure 2.15 Current sensitivity of different-trilayer TMDC heterostructure biosensors for various no. of Aspartic acid as a function of back gate voltage. Here sensitivity is defined as a ratio of currents. Therefore, sensitivity is unit less for biosensor unlike pH sensor. Highest sensitivity is found in subthreshold region for all three FETs. $\text{MoS}_2/\text{WSe}_2/\text{MoS}_2$ and $\text{MoS}_2/\text{MoSe}_2/\text{MoS}_2$ FET show similar sensitivity for wide range of gate voltages while $\text{MoS}_2/\text{WS}_2/\text{MoS}_2$ FET shows least sensitivity among them, notably in subthreshold region. 30

Figure 3.1 (Left) Schematic initial structure of Junctionless DM-DG-MOSFET biosensor. Different parameters considered here are as follows, $T_{bio} / T_{ox} = 9$ nm with 1 nm Native SiO_2 , $T_{ch} = 10$ nm, $L_1=10$ nm, $L_2=30$ nm, $L_3=L_4=5$ nm. Doping in source, drain and channel is $1 \times 10^{25} \text{ m}^{-3}$. (Right) (b) Comparison of surface potential obtained from analytical model and ATLAS simulation for the device in left.....	33
Figure 3.2 2D view (side) of Figure 3.1. Here Region IV is connected to drain.....	41
Figure 3.3 Variation of sensitivity factor ΔV_{th} for n-type DM-DG-MOSFETs for different positions of biomolecule in the cavity region when Region IV is connected to drain.....	41
Figure 3.4 2D view (side) of Figure 3.1. Here Region I is connected to drain.....	43
Figure 3.5 Variation of sensitivity factor ΔV_{th} for n-type DM-DG-MOSFETs for different positions of biomolecule in the cavity region when Region I is connected to drain.....	43
Figure 4.1 The MOSFET structure under consideration. It has a trilayer TMDC material channel sandwiched between top and bottom oxides and corresponding top and bottom gates. The channel, the source, and drain are highly n-doped regions of the same 2D material. Top oxide is etched one side to simulate effect of biomolecule on conductivity of the FET.	46
Figure 4.2 To establish the differential system for the 2D MOSFET an infinitesimal box is considered to which Gauss's Law ($\oint \epsilon E \cdot ds = Q$) is applied. The directions of the surface vectors are outward positive. Figure is taken from [85]	47
Figure 4.3 Potential profile when biomolecule dielectric constant is equal to top oxide dielectric constant.	50
Figure 4.4 Potential profile when biomolecule's relative dielectric permittivity is equal to 3, 5, 7 and 9.....	51
Figure 4.5 $I_d - V_G$ characteristics of dielectrically modulated trilayer TMDC FET. 53	
Figure 4.6 $I_d - V_G$ characteristics of dielectrically modulated trilayer TMDC FET. (Zoomed in subthreshold region).....	54
Figure 4.7 Sensitivity in the subthreshold region	54

List of Abbreviations

DNA	Deoxyribonucleic acid
ISFET	Ion-sensitive field-effect transistor
SiNW	Silicon nanowire
FET	Field-effect transistor
SWCNT	Single-walled carbon nanotube
GMR	Giant magneto resistance
MRI	Magnetic resonance imaging
SCEs	Short Channel Effects
DIBL	Drain Induced Barrier Lowering
TMDC	Transition Metal Dichalcogenides
MoS ₂	Molybdenum disulfide
WSe ₂	Tungsten diselenide
MoSe ₂	Molybdenum diselenide
DMFET	Dielectric modulated FET
DGFETs	Double-gated field-effect transistors
JL MOSFET	Junctionless Metal–Oxide–Semiconductor Field-Effect Transistor
DM	Dielectric Modulation
BZ	Brillouin Zone
ODTMS	Octadecyltrimethoxysilane
FG	Fluid/Front gate
CMOS	Complementary Metal–Oxide–Semiconductor
APTES	(3-Aminopropyl) triethoxysilane
JL-DM-DG-MOSFET	Junctionless Dielectric modulated Double-gated Metal–Oxide–Semiconductor Field-Effect Transistor

List of Symbols

N_{imp}	Impurity density
ϵ_{2D}	Permittivity of TMDC material
q	Electron charge
ϵ_0	Vacuum permittivity
ϵ_{ox}	Oxide permittivity
ϵ_{SiO_2}	SiO ₂ permittivity
ϵ_W	Electrolyte permittivity
ϵ_{Lipid}	Lipid permittivity
ϵ_{ODTMS}	ODTMS permittivity
ϵ_m	Membrane permittivity
ϵ_{bio}	Biomolecule permittivity
ϵ_{cavity}	Cavity region permittivity
p	Hole concentration
n	Electron concentration
Q_{OH}	Net proton charge density in site binding region
Q_{Lipid}	Charge concentration due to lipid head group
H_s^+	Proton concentration at oxide-electrolyte surface
H_B^+	Proton concentration at bulk-electrolyte
N_s	Density of surface group at the oxide electrolyte interface
K_a	Protonation constant
K_b	Deprotonation constant
N_{avo}	Avogadro Number
I_0	Electrolyte Ion concentration
K_B	Boltzman Constant
N_m	Amino Acid density
V_{FG}	Front gate voltage
V_{BG}	Back Gate voltage

n_+	Cation concentration in electrolyte
n_-	Anion concentration in electrolyte
W	Sensor Width
L	Sensor Length
t_{top}	Top gate oxide thickness
t_{bottom}	Bottom gate oxide thickness
t_{TMD}	TMD channel material thickness
N_D	Channel Doping Density
μ_{eff}	Effective carrier mobility
C_i	Gate capacitance per unit area of the gate dielectric
V_{bi}	Built in potential
n_i	Intrinsic carrier concentration
I_{dsub}	Current in subthreshold region
V_{DS}	Drain Voltage
σ_{OH}	Net charge of surface group per area of the top oxide surface
C_{tox}	Top oxide Capacitance
C_{box}	Bottom oxide Capacitance
T_{bio}	Thickness of Biomolecule
T_{ox}	Thickness of Oxide
T_{ch}	Thickness of Channel
N_f	Biomolecule charge density
N_a	Doping concentration of acceptor impurity
N_d	Doping concentration of donor impurity
$\phi_i(x, y)$	2-D potential distribution in the Silicon channel
$\phi_{\text{fsi}}(y)$	Front gate surface potential
$\phi_{\text{bsi}}(y)$	Back gate surface potential
$\phi_{\text{ci}}(y)$	Central potential

Chapter 1

Introduction

1.1 The Rationale of ‘Nano-scale’ Sensors

Cancer is one of the leading causes of premature morbidity and mortality in the developed world, accounting for up to 12% of all deaths[1]. At present, cancers are often diagnosed late in the course of the disease since available diagnostic methods are not sufficiently sensitive and specific. For example, although the prognosis for lung cancer patients is poor with 5-year survival rates being less than 10%, the 5-year survival rate increases dramatically to 52% only if patients are diagnosed sufficiently early in the disease process and treated promptly by surgery[2]. Thus, the ideal goal of screening for various cancers is to detect the disease at an early phase when it is curable.

The widely acknowledged benefits of early diagnosis have prompted research into methods of screening for early stage cancers. So far, the detection of cancers in the clinic has been relied on the detection of biomarkers (proteins indicating the presence of specific cancers in human body) with laboratory tests such as enzyme-linked immunosorbent assay (ELISA)[3]. Despite considerable advances in protein detection, the current ELISA-based detection methods have several drawbacks: (i) the limit of detection is around nM (10^{-9} M) down to pM (10^{-12} M) regime at their best, which is still not enough for the early detection and screening of cancers, (ii) its incubation time is several hours or even up to a day, (iii) the cost-inefficient pre-processing of samples since the tagging of antibodies with fluorescent dye is required, and (iv) inherent autofluorescence or optical absorption of biological samples contaminate its fluorescent or colorimetric signal.

During the last decade, one-dimensional, nanoscale sensors have attracted a huge interest in the field due to their extraordinary sensitivity, label-free detection, and potential for the integration with classical microelectronic technology. The fundamental reasons for driving to the nanometer-sized materials/devices are based on the two major properties: (i) they are comparable in size with most biological entities like DNA, protein and viruses (Figure 1.1) thus they can be the ideal transducer between biomolecules and measurement instruments and that (ii) their high surface-to-volume ratio (S/V) makes them sensitive to the changes in their ambient conditions.

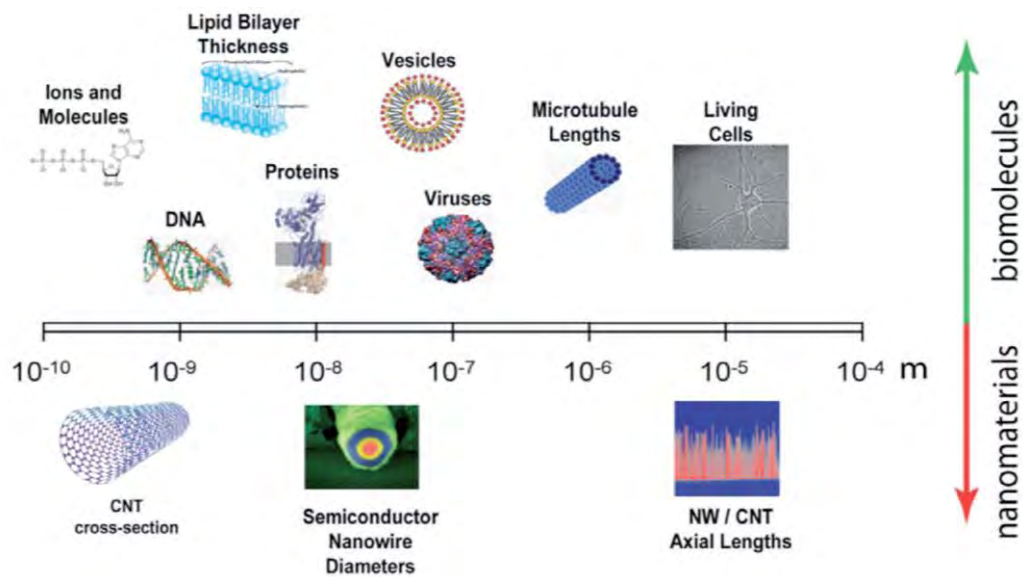


Figure 1.1 Comparative size of some key biological structures and nanomaterials[4].

These biological diseases, however, are not the only threat to the human health: Indeed, there exists a broad range of environmental threats from toxic industrial chemicals and materials that affect human health adversely and must be detected by sensors.

1.2 Mechanisms of Detection: Biosensors vs. Chemical Sensors

A biosensor is an analytical tool consisting of biologically active material (e.g., DNA, proteins, etc.) used in close conjunction with a device that converts a biochemical signal into a quantifiable electrical signal. A biosensor has two components: a receptor and a transducer[5]. The receptors are responsible for the selectivity of the sensor (e.g., enzymes, antibodies, and lipid layers). The transducer translates the physical or chemical change by recognizing the analyte and relaying it through a signal. Figure 1.2 describes a typical biosensor configuration that detect the target analyte with receptors. The device incorporates a bimolecular sensing element with a traditional transducer. The biological-sensing element selectively recognizes a particular biological molecule through a reaction, specific adsorption, or other physical or chemical process, and the transducer converts the result of this recognition into a quantifiable signal. Common transduction mechanism are based on optical, electro optical or electrochemical signals; this variety offers many opportunities to tailor biosensors for specific applications.

Chemical sensors, on the other hand, are different compared to biosensors: First, the phase of target molecules / sensing environment is not liquid (like biosensing) but gas. While the biomolecules have electric charges in the fluid environment, the chemicals in gas phase are

charge-neutral. In addition, most importantly, there is no analytic specific lock-and-key receptors in chemical sensors. Often this can be advantageous as few receptors can interpret signals from broad range of sources.

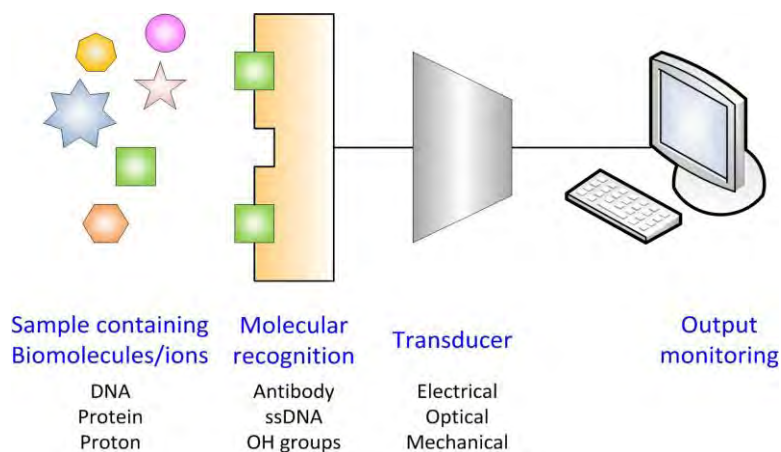


Figure 1.2 A conceptual diagram of a biosensor composed of recognition module and transducer.

1.3 Technologies in Biosensing

In this section, we classify modern biosensors and introduce their basic features according to the nature of transduction mechanism. We cover recent achievements in biosensing technology based on some major transduction mechanisms like electronic and magnetic detection.

1.3.1 Electronic Detection

One of many possible ways to implement the signal transducer is to use electronic devices and monitor the changes in their conductance because of the interaction with biomolecules nearby. Ions or biomolecules (such as DNA or proteins) have their own net charge in electrolyte solution, and their electrical interaction with transducers allows us to detect them[6]. In 1970, Bergveld first suggested that the electronic pH sensing can be achieved with ion-sensitive field-effect transistors (ISFETs), promising the microscale, integrated biosensors for multiplexed detection of target molecules[7][8]. It has been demonstrated that silicon nanowire (SiNW) biosensors[9] or nanotubes[10] offers greatly enhanced sensitivity in the electronic biosensing (Figure 1.3) compared to the conventional planar ISFETs. The most important and powerful advantage of SiNW sensors is the possibility of label-free, multiplexed, and real-time detection. The underlying mechanism of nanowire sensors is based on the principle of field-effect transistors (FETs). For biosensors, binding of a charged species on the surface of the SiNWs is analogous to applying a gate voltage. By monitoring the conductance change, the binding of

targets to probe molecules can be detected on the Si surface. CNTs also could be considered an ideal material for sensing applications since every atom in a single-walled carbon nanotube (SWNT) is located on the surface, leading to extreme sensitivity to the surrounding environment.

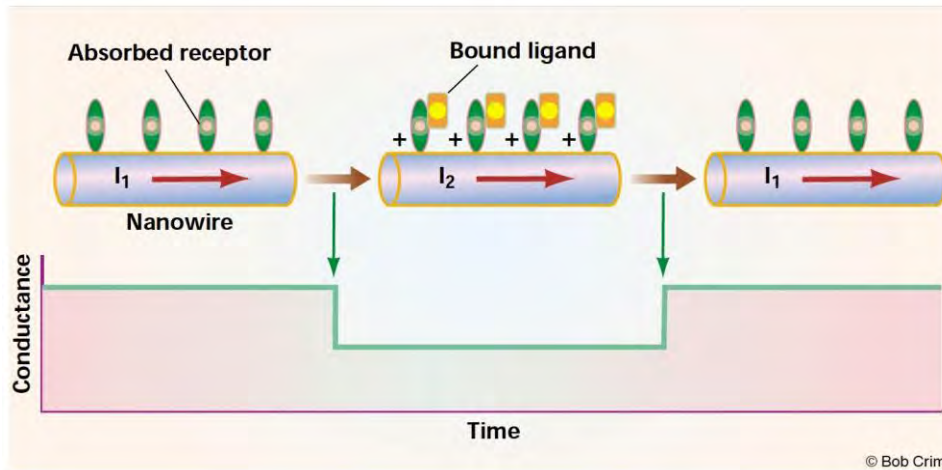


Figure 1.3 Electronic detection scheme with SiNW biosensors. Introduction of target molecules causes a change in conductance across the nanowire. The conductance returns to its initial level after rinsing with buffers[11].

The current detection sensitivity of SiNW/CNT is in the range of fM[9], which is several orders of magnitude more sensitive than a conventional ELISA assay. The major drawback of electronic detection is, however, the screening effect of charged target molecules due to the presence of their counter ions in solution[12]. Avoiding the electrolyte screening effect requires additional processing costs such as dilution of buffer solutions[9], introduction of electro-diffusion flow in electrolyte before detection[13] etc.

1.3.2 Magnetic Detection

Magnetic detection methods have been suggested in the literature as a preferred alternative to electronic detection, which fundamentally suffers from the electrolyte screening. In electronic detection, various types of background electronic noise, such as ions in electrolyte and OH group on the sensor surface, hinders the sensitive detection. Most biological samples, on the other hand, lack a detectable magnetic background signal and do not interfere with the magnetic transduction mechanism. Therefore, a magnetic field-based detection platform is well suited for biomolecule detection in clinical samples. Gaster et al. demonstrated a giant magneto resistive (GMR)-based biosensor with its detection limit

down to the attomolar level as well as its real-time detection capability[14]. Another method that has achieved considerable success is based on magnetic resonance (MRI/NMR), which involves using magnetic nanoparticles as proximity sensors[15].

1.4 Next Generation Potentiometric Biosensor

In this section, we will talk about the technologies proposed as alternative to current Si technology and the biosensors based on these technologies.

1.4.1 Switching to 2D materials and heterostructures

As technology node gets smaller, gate length and oxide thickness get smaller as well, leading to Short Channel Effects (SCEs) and gate leakage current. The most common short channel effects are Channel Length Modulation, Drain Induced Barrier Lowering (DIBL), Threshold Voltage Roll-off and Velocity Saturation. Over the years, the semiconductor industry had come up with various modifications to the basic Si-based MOSFET structure to keep those non-ideal effects in check and continue scaling.

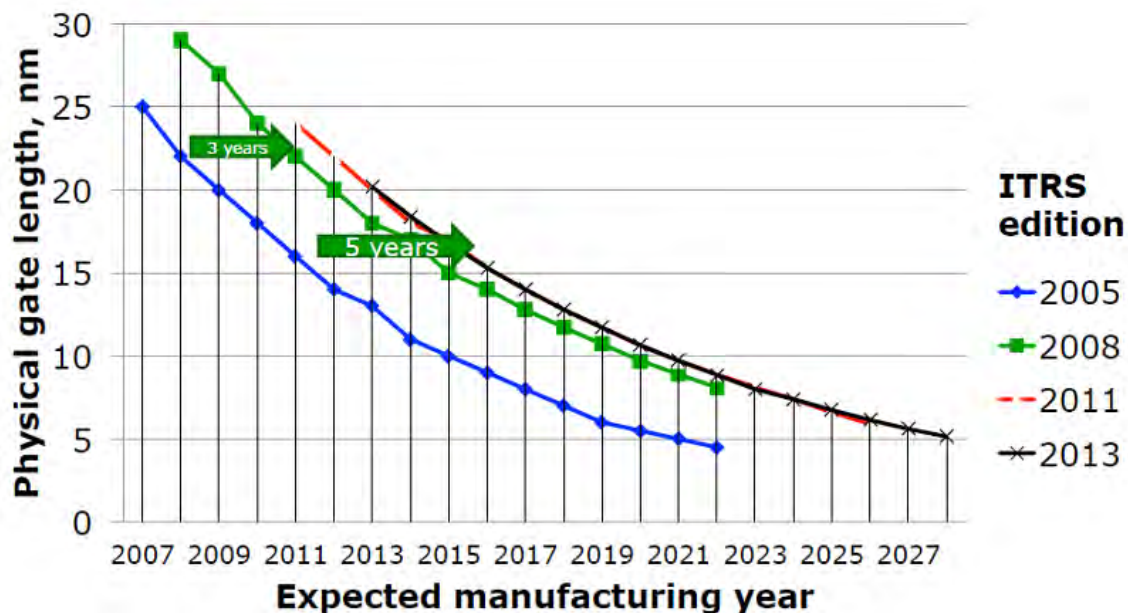


Figure 1.4 ITRS roadmap[16] for transistor scaling in terms of physical channel length.

From 2011, Intel started to use Tri-gate Silicon transistors in their 22 nm technology nodes, allowing them to have better gate control on the device channel and reduce the SCEs. Intel will

be using the same Tri-gate Silicon transistors technology in their upcoming processors beyond the 22 nm node.

As technology node goes down to 10 nm, 7 nm and eventually to 5 nm, to keep up with the Moore's law the physical gate length of the transistors needs to be shrunk as well. By the year 2028, the physical gate length of transistors will be 5 nm (Figure 1.4) which means only around 10 Silicon atoms in the channel. Beyond 10 nm node, Tri-gate Silicon channel transistors will not suffice to overcome the power dissipation and scaling challenges and new materials and structures will be needed. Intel's Innovation Enabled Technology Pipeline (Figure 1.5) supports the need for alternate channel materials and novel structures for future generation transistors.

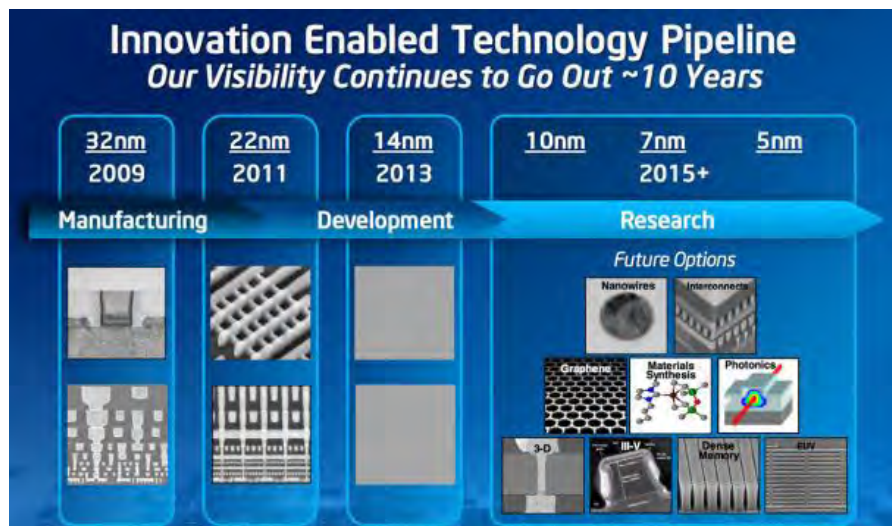


Figure 1.5 Intel's innovation enabled technology pipeline info graphic.

To overcome the electrostatics and power challenges global research efforts have been devoted by researchers to innovate new materials for semiconductor application. These materials range from Organic Materials, III-V Compound Materials, Graphene and other 2D materials. Along this line of effort came the innovation of Monolayer Transition Metal Dichalcogenides (TMDCs) as prospective candidates for the next generation of transistors.

Two-dimensional materials such as Transition Metal Dichalcogenides (TMDC) and their bi-layer/tri-layer heterostructures have become the focus of intense research and investigation in recent years due to their promising applications in electronics and optoelectronics. Layered van der Waals materials, such as metal dichalcogenides, few layers thick or exfoliated down to single layer, have become subject of extensive research in recent times [17][18]. *Ab-initio* simulation on electronic structures of monolayer TMDC materials reveals tunability in bandgap

and electronic effective mass at conduction band minima under biaxial strain application [19][20]. Stacking multiple layers of on top of each other of these materials also leads to interesting changes in electronic properties [21][22][23]. Presence of intrinsic bandgap of monolayer and multilayer 2D materials, tunability of electronic properties with layer thickness, lower rate of electronic mobility degradation with dimensional scaling, and scalability down to monolayer dimension makes these materials suitable for electronic device application. Although MoS₂ is the most widely studied and investigated [24][25] [26] TMDC material, high performance MOSFETs have been implemented with other TMDC materials as well [27][28]. Recently, several studies have been performed on the modeling and projection of 2D FETs for sub-10 nm VLSI applications, further emphasizing their potential for ultra-scale high-performance electronic devices [29][30][31]. Electronic devices based on 2D bilayer heterostructures have been studied and investigated [32][33][34] also. Besides bilayer 2D heterostructures, trilayer TMDC heterostructures based on MoS₂ have also been studied using first principle simulations [35].

1.5 Motivation for choosing trilayer TMDC for biosensor operation

In recent years, owing to the fast advances in nanotechnology, label-free biosensors based on nanoscale materials and structures with novel properties have been demonstrated, which outperformed the traditional methods in almost all aspects of a biosensor, such as detection speed, sensitivity, cost, and versatility. However, synthesizing biosensors that simultaneously meet all these criteria has proven challenging. Although one-dimensional (1D) semiconductors, such as semiconductor nanowires[13] and carbon nanotubes[10] are usually the preferred channel materials for field-effect transistor (FET)-based biosensors, the emerging two-dimensional (2D) graphene sheets are also explored due to their large active surface area, which enhances the adsorption of target molecules, and their extreme thinness (only one atom thick)[36][37] which enables low-noise operation. However, graphene lacks bandgap, which adds a large leakage current and reduces dynamic range of the sensor. Other 2D nanomaterials such as transition metal dichalcogenides, for example, molybdenum disulfide (MoS₂) have also attracted significant research interests. In contrast to graphene, MoS₂ has a direct energy bandgap that significantly lowers the leakage current. Fabrication of MoS₂ Nano sheet-based field effect transistors as NO gas sensor[38] and chemical vapor sensor have been reported[39]. MoS₂ based FET are thus expected to be a potential candidate for biosensing[40].

MoS₂, one of transition metal dichalcogenides (TMDCs), has been studied as an attractive nanoelectronic material for making field-effect transistor (FET) biosensors[41] because the

transport characteristics of monolayer or few-layer MoS₂ FET channels are extremely sensitive to external stimulations, such as antigen-antibody binding events; 2D MoS₂ surfaces have an extremely low density of electron scattering centers, which can result in a low detection noise; and also semiconducting MoS₂ FETs exhibit much higher $\frac{On}{Off}$ ratios and therefore the higher detection sensitivities in comparison with semi-metallic graphene FETs[42]. Therefore, MoS₂ FET biosensors hold the significant potential to enable single-molecule-level (or fM-level) detection of illness-related biomarkers. To leverage such superior sensing capability of MoS₂ FETs for cost-efficient immunoassay applications, large-scale MoS₂ FET arrays need to be manufactured at an affordable cost. To minimize the manufacturing cost, the sensor structure should be as simple as possible while meeting requirements unique to biosensing[43].

1.6 Some Experimental Setups of TMDC Sensor

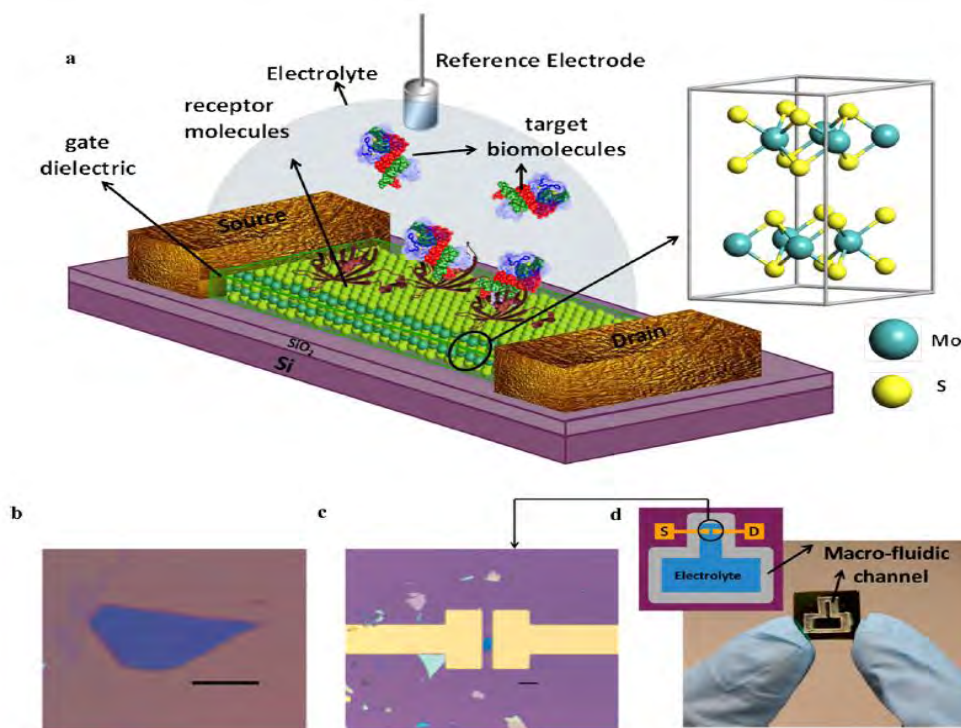


Figure 1.6 MoS₂-based FET biosensor device. (a) Schematic diagram of MoS₂-based FET biosensor. For biosensing, the dielectric layer covering the MoS₂ channel is functionalized with receptors for specifically capturing the target biomolecules. The charged biomolecules after being captured induce a gating effect, modulating the device current. An electrolyte gate in the form of a Ag/AgCl reference electrode is used for applying bias to the electrolyte. The source and drain contacts are covered with a dielectric layer to protect them from the electrolyte (not shown in this figure). (b) Optical image of a MoS₂ flake on 270 nm SiO₂ grown on degenerately doped Si substrate. Scale bar, 10 μ m. (c) Optical image of the MoS₂ FET biosensor device showing the extended electrodes made of Ti/Au. Scale bar, 10 μ m. (d) Image and schematic diagram (inset figure) of the chip with the biosensor device and microfluidic channel for containing the electrolyte. Inlet and outlet pipe for transferring the fluid and the reference electrode are not shown in the figure(Courtesy [41]).

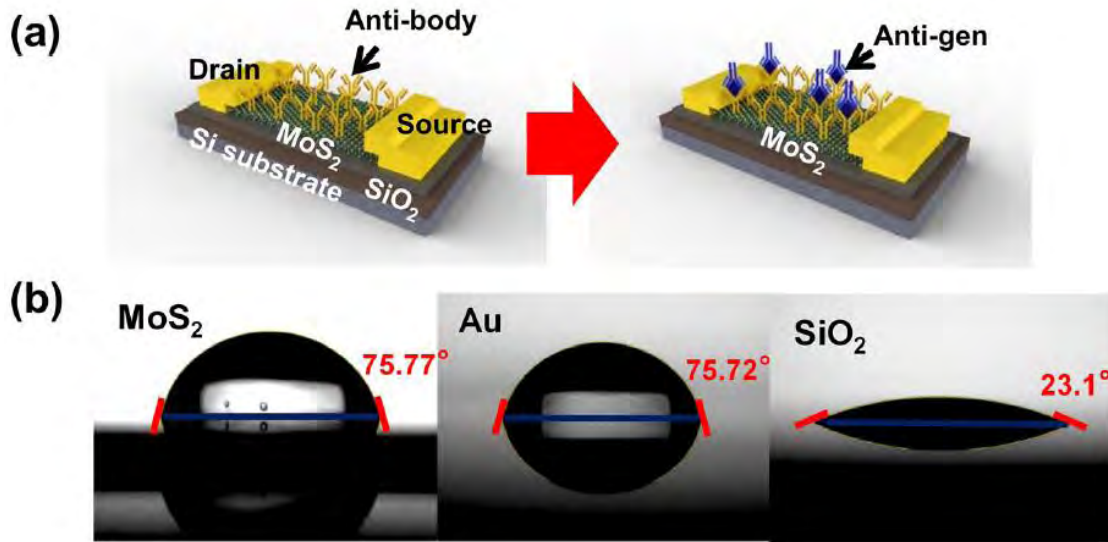


Figure 1.7 A MoS₂ nanosheet biosensor and contact angles of different surfaces. (a) Schematic of a MoS₂ biosensor configured as a PSA, detecting label free immunoassay, illustrating PSA antibody functionalized MoS₂ surface (top) and subsequent binding of PSA antigen with antibody receptors. The MoS₂ nanosheet biosensor consists of a gate insulator of SiO₂ (300 nm) and a drain-source metal contact of Ti/Au (15nm/300 nm) (b) The water contact angle measurement to confirm hydrophobic characteristics of different substrates: the water contact angle of MoS₂, Au, and SiO₂ substrate are 75.75, 75.72, and 23.1 degree, respectively. The contact angle of MoS₂ surface, which is more hydrophobic than Si-based substrates, is comparable to that of Au surface. This suggests that MoS₂ nanosheet is an excellent candidate for functionalizing antibody and protein due to its hydrophobic surface. (Courtesy [44])

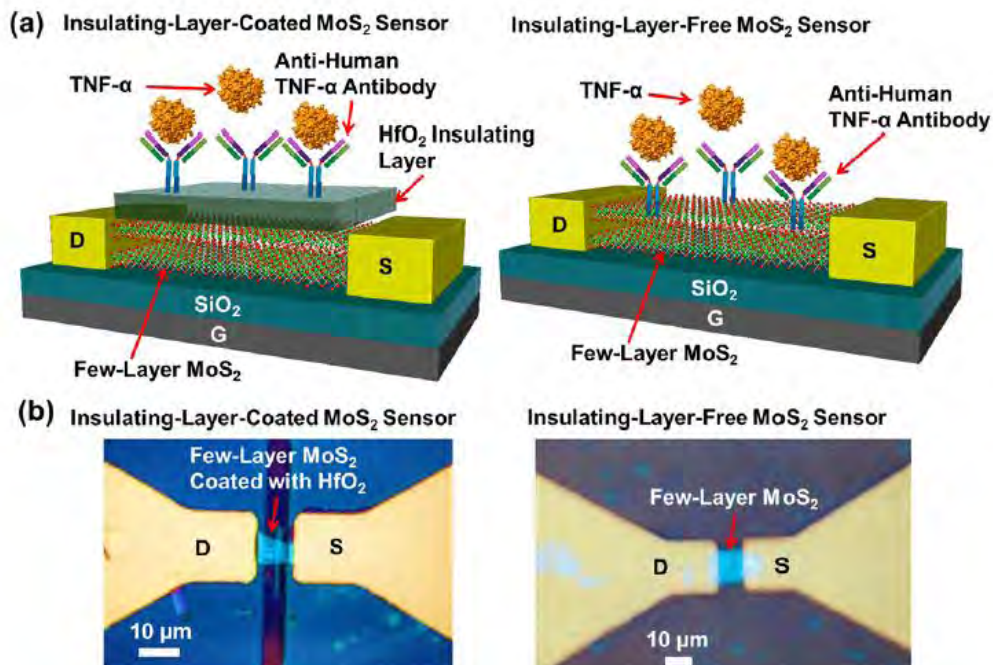


Figure 1.8 Illustrations (a) and optical micrographs (b) of insulating-layer coated (left) and insulating-layer-free (right) MoS₂ FET biosensors [43].

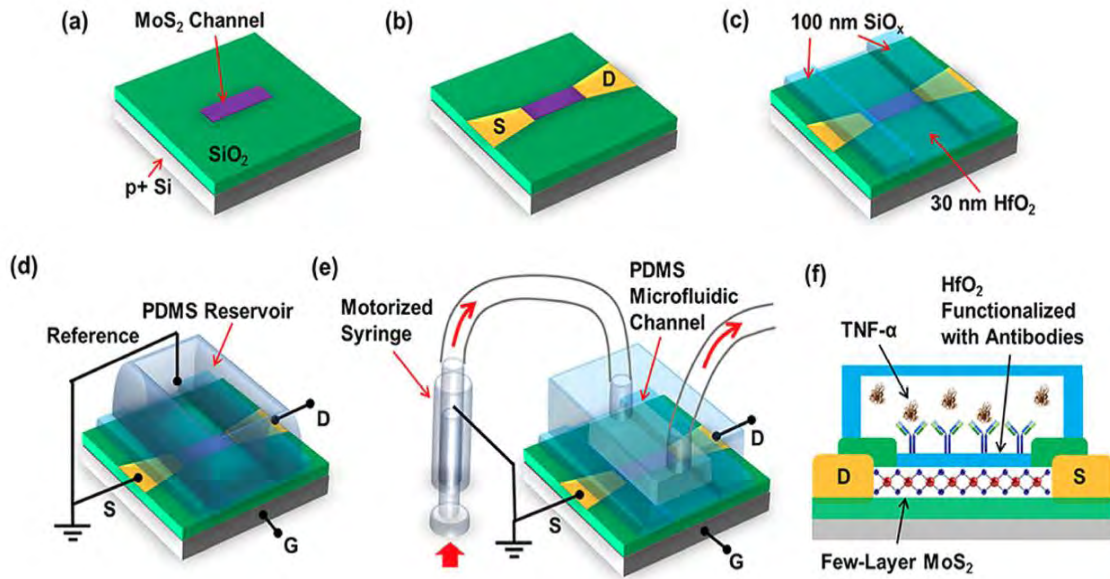


Figure 1.9 Flow chart for fabricating a MoS₂ transistor biosensor: (a) printing of a few-layer MoS₂ flake onto a substrate; (b) fabrication of Ti/Au D/S contacts; (c) ALD growth of the HfO₂ effective layer on top of the MoS₂ channel and coating of D/S contacts with thick SiO_x layers; (d) integration of a PDMS liquid reservoir on top of the MoS₂ transistor for measuring sensor responses from different TNF concentrations under thermodynamic equilibrium condition and determining the affinity of the antibody-(TNF- α) pair; (e) integration of a microfluidic inlet/outlet tubing kit driven by a motorized syringe pump on top of the transistor (f) functionalization of the HfO₂ effective layer with antibody receptors and subsequent TNF- α detection (Courtesy [45]).

1.7 Dielectrically Modulated Junctionless FET

With the inception of ion-sensitive field-effect transistors (ISFETs) in 1970[46], ISFET and its derivatives became popular for electrical detection of charged biomolecules, but it lacks in the detection of neutral biomolecules. Thereafter, the concept of dielectric modulated FET (DMFET) was proposed[47], with nanogap cavity at both source and drain ends enabling the label-free detection of neutral biomolecules as well with high sensitivity. Kim *et al.* reported a DMFET for the label-free DNA detection technique[48], taking into consideration both the dielectric constant and the charge possessed by a biomolecule.

1.8 Thesis Objectives

The objectives of this work are:

- a. To develop a self-consistent simulator to calculate spatial charge and electrostatic potential distributions within FET based sensor for pH and biomolecule detection in addition, optimization of its detection capability.
- b. To develop an analytical model for surface potential in Junctionless Field Effect Transistor based biosensor and verification through standard simulations.

1.9 Thesis Organization

The entire thesis is organized into five chapters. A brief outline of each chapter is described below.

The first chapter briefly discusses the technologies of biosensing with the short summary on revolution of FET based potentiometric nanobiosensor. The chapter focuses the need to go for next generation multilayer TMDC biosensor. The chapter ends with the some recent experimental results on MoS₂ sensor.

We propose the application of double-gated field-effect transistors (DGFETs) as pH and biosensors in Chapter 2 with the channel material intercalated trilayer TMDC being considered. We consider the electrostatics of the system that involves nanoscale silicon body surrounded by top and bottom oxide, electrolyte biomolecules, fluid gate and back gate. We predicted the detection of aspartic acid as an example and demonstrated the signal amplification depending on their operation modes. The effect of geometry parameters as well as the material characteristics are also addressed.

In chapter 3, an analytical model for Junctionless (JL) Metal–Oxide–Semiconductor Field-Effect Transistor (MOSFET) based biosensor for label free electrical detection of biomolecules like enzyme, cell, DNA etc. using the Dielectric Modulation (DM) technique has been developed. The analytical results are validated with the help of ‘SILVACO ATLAS’ device simulation software. For the biomolecule immobilization, nanogap cavity is formed in the JL MOSFET by etching gate oxide layer from both source as well as drain end of the channel. As a result, the surface potential in the channel underneath the nanogap cavity region is affected

by the neutral and charged biomolecules that binds to SiO_2 adhesion layer in the cavity. The surface potential is obtained by solving a 2-D Poisson's equation assuming parabolic potential profile in the channel. The shift in threshold voltage of the device has been considered as the sensing metric for detection of biomolecules under dry environment condition.

Chapter 04 provides the same analysis but now the channel material is trilayer transition metal dichalcogenide. Since the material is only two nanometer thick, bulk material analysis will not be valid this time. We have adopted Gauss law equation to turn the physics inside a TMDC nanobiosensor into differential equations and useful results follow this.

The fifth and last chapter of this thesis outlines the conclusion of this thesis work. It also briefly describes prospective fields of future improvements and modifications to this work.

Chapter 2

Simulation Study of Electrical Response of Multilayer TMDC Nanobiosensor in Wet Environment

2.1 Electronic Properties of Trilayer Transition Metal Dichalcogenides

In this work, we have used $\text{MoS}_2/\text{MX}_2/\text{MoS}_2$ ($M=\text{W}$ or, Mo ; $X=\text{S}$ or, Se) trilayer heterostructures as channel materials. The configuration of the trilayer material is shown in Figure 2.1. For the electronic structure simulation, pw.x package of the open source simulation framework Quantum Espresso have been used[49]. At first, geometric structure of the trilayer unit cell was relaxed until the force on each atom in each direction was less than 10^{-3} Ry/au. The self-consistent convergence criterion for energy was kept fixed at 10^{-9} Ry. For geometry optimization and energy calculation of the electronic structure, scalar relativistic norm-conserving pseudopotential with Perdew–Burke–Ernzerhof (PBE) exchange correlation functional [50] has been used in the literature. The complete simulation method described here and result of the material study have been summarized from [51].

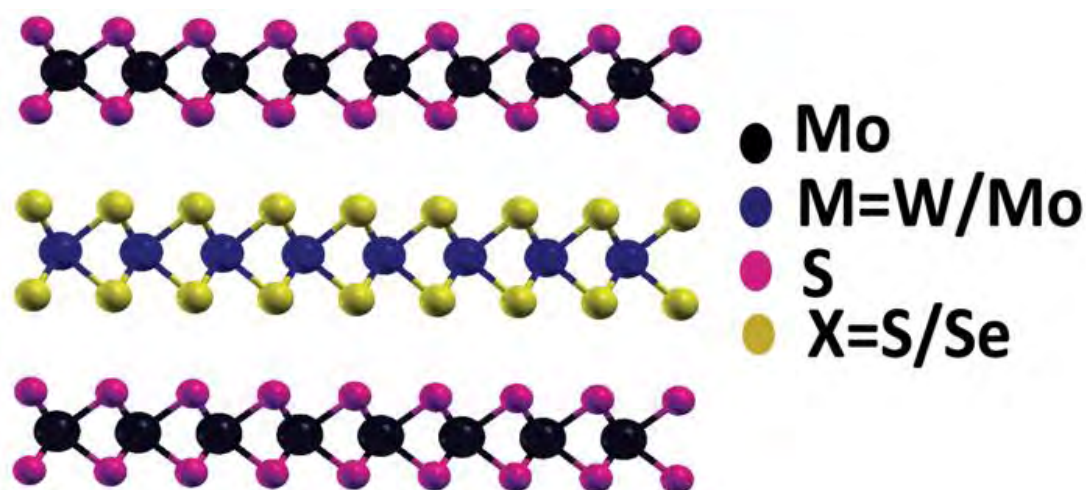


Figure 2.1 $\text{MoS}_2/\text{MX}_2/\text{MoS}_2$ trilayer structure used in this study.

The Brillouin Zone (BZ) sampling was done using a Monkhorst–Pack scheme of $24 \times 24 \times 1$ points for electronic structure calculation [52]. After structural optimization and ground state energy calculation, band structure of the trilayer structure using the bands.x package is calculated. The dielectric constant for the trilayer lattice structure was calculated using ph.x

package of Quantum Espresso. The results obtained from electronic structure simulation on the trilayer heterostructures under relaxed condition is given in Table 2.1.

Table 2.1 Extracted Values of Effective Mass at Conduction Band Minima, Bandgap, Dielectric Constant from First Principle Simulation[51]

Material	Effective Mass (m_0)	Bandgap (eV)	Dielectric Constant (ϵ_0)
MoS ₂ /MoSe ₂ /MoS ₂	0.5126	0.707	$\epsilon_{xx}=6.99$
			$\epsilon_{yy}=6.99$
			$\epsilon_{zz}=1.52$
MoS ₂ /WSe ₂ /MoS ₂	0.5035	0.45	$\epsilon_{xx}=6.84$
			$\epsilon_{yy}=6.84$
			$\epsilon_{zz}=1.53$
MoS ₂ /WS ₂ /MoS ₂	0.5753	1.3	$\epsilon_{xx}=6.50$
			$\epsilon_{yy}=6.50$
			$\epsilon_{zz}=1.51$

2.2 Model System

Figure 2.2 shows the schematic of the proposed double gate FET used in this work as pH sensor and biosensor respectively. Trilayer TMDC heterostructure as channel material with thicknesses around 2 nm is used. SiO₂ has been used as gate dielectric on both sides of the channel for this work. However, the simulation procedure used in this work can take into account of various dielectrics. In case of pH sensing, fluid/front gate voltage, V_{FG} is kept 1V for all simulations while Back gate voltage, V_{BG} is changed from 1V to 5V for operation over the Nernst limit. Thickness of both top gate and bottom gate oxide is varied for pH sensing.

Beside pH sensing, we also discuss the application of the proposed trilayer materials as channel material in a potentiometric Nano biosensor for protein detection. The device prototype in Figure 2.2(right) has been inspired from[53] where the original channel material Si is replaced by the TMDC heterostructure. The device is incorporated with proper receptors to provide a more realistic conclusion than the simple approach used in [54].

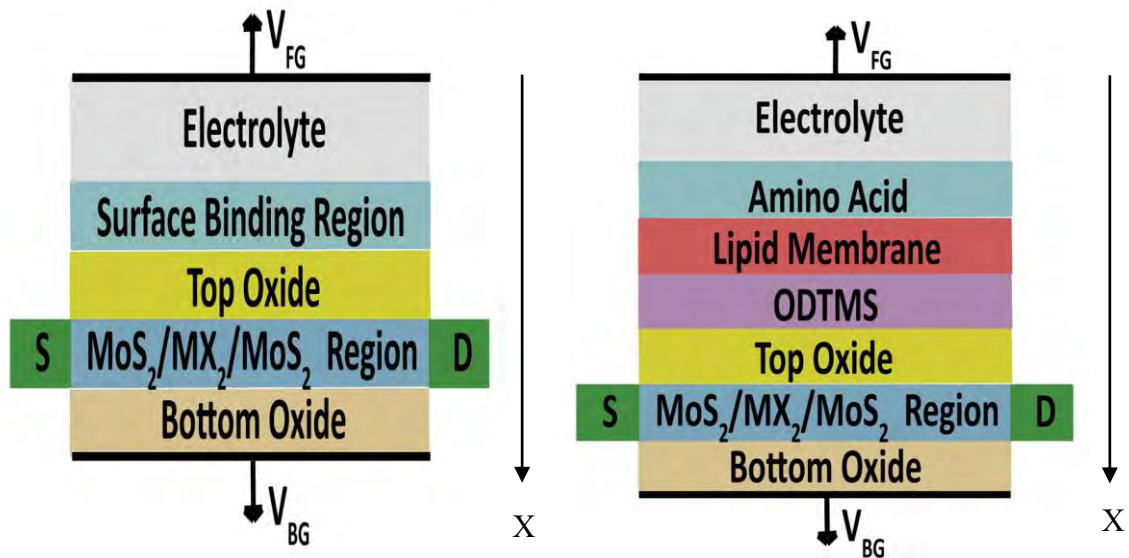


Figure 2.2 Simple Schematic representations of the pH sensor (left) and Biomolecule (Amino Acid) sensor (right) used in this paper. Here SiO_2 is used as top and bottom oxide for pH and biosensor. None of the devices shown in this figure is drawn to scale.

We have considered an artificial protein structure (Aspartic acid) where amino acids are tagged to a histidine chain. A part of this artificial protein remains uncharged since no amino acids are attached there. By contrast, the rest of the histidine backbone is negatively charged since we consider Aspartic acids that carry one negative charge each for binding to the tag. In this work, the charge of the aspartic acids has been varied from a single charge up to nine charges. Therefore, for different Aspartic acids, we will get a different surface charge density that will cause a change in sensor's response. The electrolyte region includes the histidine-tagged aspartic acids as well as the neutral part of the tag. Thickness of both top and bottom oxide is kept constant (top oxide 2 nm and bottom oxide 20 nm) to values for which measurable change in device current is found for change in the number of Aspartic acid. The top oxide layer is passivated by an ODTMS (octadecyltrimethoxysilane) monolayer, required for the bio-functionalization of the semiconductor device. Widths of ODTMS, lipid membrane, and neutral part of histidine tag have been considered 1.6 nm, 2.0 nm and 2.8 nm respectively. No interface trap is present in top oxide-electrolyte interface because of the functionalization by ODTMS. For this reason, we are not considering any site-binding charges in this case and therefore, no pH sensing is possible with this structure. Lipid membrane has been used as surface functionalization upon ODTMS layer, which acts as receptor for the histidine tagged Aspartic acid. Material parameters for lipid membrane is kept same as those of ODTMS. Since the lipid membrane layer is highly dense, no electrolyte is present within this layer. We have

considered an electrolyte ion concentration of 30mM. For all calculations, the pH of the bulk electrolyte has been set to seven.

2.3 Model Equations

Consider DGFET sensors shown in Figure 2.2. We use a semiclassical approach to model the electrostatics of ISFET-DGFET sensor. In each region of the system, we set up different models and solve the equations according to the given boundary conditions. For the following analysis, the DGFET can be divided into several different regions (associated equations are provided in Table 2.2): (i) fluid gate-electrolyte interface, (ii) the electrolyte, (iii) the top oxide-electrolyte interface, (iv) the FET system (composed of trilayer TMDC and oxide layers), and (v) the receptor for attaching biomolecules. In addition, the symbols and the numerical values used in this chapter are summarized in Table 2.3. We now describe the physical motivation of using these specific equations in some detail.

Table 2.2 Equations Governing the Electrostatics of the DGFET Sensor

Region	Equation
TMDC (Channel)	$-\nabla \cdot (\epsilon_{2D} \nabla \Phi) = q(p - n + N_{imp})$ $N_{imp} = \text{Impurity density}$
Top and Bottom gate Oxide	$-\nabla \cdot (\epsilon_{sio_2} \nabla \Phi) = 0$
Top oxide-electrolyte interface (Site binding region) (Only for pH sensor)	$(\epsilon_{sio_2} \nabla \Phi_{at\ x=0-}) - (\epsilon_w \nabla \Phi_{at\ x=0+}) = Q_{OH}$ $\epsilon_w = 80 * \epsilon_0$ $Q_{OH} = qN_s([OH_2^+] - [O^-])$ $N_s = 5e14, (K_a, K_b) = (-2,6)$
ODTMS (Only for Biomolecule Sensing)	$-\nabla \cdot (\epsilon_{ODTMS} \nabla \Phi) = 0$
Lipid Membrane (Only for Biomolecule Sensing)	$-\nabla \cdot (\epsilon_{Lipid} \nabla \Phi) = Q_{Lipid}$ <p>Q_{lipid}=charge concentration due to lipid head group</p>
Amino Acid (Only for Biomolecule Sensing)	$-\nabla \cdot (\epsilon_w \nabla \Phi) = \frac{2q^2 N_{avo} I_0}{K_B T} \sinh\left(\frac{q(\phi - V_{FG})}{K_B T}\right)$ $+ qvN_m$ $v = \text{Amino Acid charge per unit length}$

	$N_m = \text{Amino Acid density}$
Electrolyte	$-\nabla \cdot (\epsilon_w \nabla \Phi) = \frac{2q^2 N_{avo} I_0}{K_B T} \sinh\left(\frac{q(\phi - V_{FG})}{K_B T}\right)$ $I_0 = 50mM$ $N_{avo} = 6.023 \times 10^{23} \quad n_0 = N_{avo} I_0$

(i) Fluid gate-Electrolyte Interface: An important assumption made the traditional model is that the reference electrode is faradaic: A faradaic electrode can exchange electrons with ions in electrolyte such that there is no potential drop at the electrode-electrolyte interface, and the electrostatic potential applied at the electrode drops fully at the other side (the sensor surface in case of ISFET) of the electrolyte, so that the electrostatic potential in the bulk electrolyte as well as at the electrode-electrolyte interface is fixed:

$$\Phi = V_G \quad (2.1)$$

(ii) Electrolyte System: The ions in bulk electrolyte are assumed 1:1 (such as NaCl or KCl) and the distribution of cations (n_+) and anions (n_-) follows the Boltzmann distribution:

$$\begin{aligned} n_+ &= n_0 \exp\left(-q(\Phi - V_{FG}) / k_B T\right) \\ n_- &= n_0 \exp\left(+q(\Phi - V_{FG}) / k_B T\right) \end{aligned} \quad (2.2)$$

Where n_0 is the bulk electrolyte concentration (see Table 2.2), k_B is the Boltzmann constant, and T is the temperature. Note the coupling of the fluid-gate bias within the exponents. The Poisson equation is used to calculate the overall potential within the electrolyte system, as shown below:

$$-\nabla(\epsilon_w \nabla \Phi) = q(n_+ - n_-) \quad (2.3)$$

Table 2.3 Sensor Parameters

Definition	Symbol	Default value
Sensor Width	W	100 nm
Sensor Length	L	10 μ m
Top gate oxide thickness	t_{tox}	2 and 4 nm
Bottom gate oxide thickness	t_{box}	6, 8 and 10 nm
Trilayer TMD thickness	t_{TMD}	2 nm
Trilayer TMD doping density	N_{imp}	Undoped
effective carrier mobility	μ_{eff}	100 cm^2/Vs
Drain voltage	V_{DS}	0.1 V
Vacuum permittivity	ϵ_0	$8.854 \times 10^{-14} F/cm^2$
Oxide permittivity	ϵ_{ox}	$3.9 \times 8.854 \times 10^{-14} F/cm^2$
Electrolyte permittivity	ϵ_W	$80 \times 8.854 \times 10^{-14} F/cm^2$
Protonation constant	pKa	-2
De-protonation constant	pKb	6
Electrolyte strength	I_0	30 mM

Conventionally, the Poisson-Boltzmann equation is linearized which leads to the Debye-Hückel approximation. However, such a simplification is generally not applicable in real devices and only valid for special and very limited cases. Instead, we solve the equation self-consistently to obtain the profile of the electrostatic potential, Φ .

(iii) ODTMS: This layer is added for biomolecule recognition. No electrolyte is present here considered. No charge is present in this layer.

$$-\nabla \cdot (\epsilon_{ODTMS} \nabla \Phi) = 0 \quad (2.4)$$

(iv) LIPID Membrane: Like ODTMS, this layer is also used for sensing biomolecules (in this case Amino Acid). Since lipid is very dense, no electrolyte is present here. Material parameters for Lipid Membrane have been used same as that of ODTMS. The functionalized surface exposes NTA head groups that carry two negative charges to the electrolyte solution. They have the ability to form a chelate complex with Positive i.e. nickel ions if the latter are present in the solution. Upon loading with positive ion in the solution, the charge of the head group changes by +1e and is then considered to be -1e.

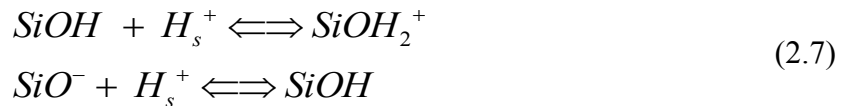
$$-\nabla \cdot (\epsilon_{Lipid} \nabla \Phi) = Q_{Lipid} \quad (2.5)$$

(v) Amino Acid (Biomolecule): The Poisson-Boltzmann equation for a biological membrane is

$$\begin{aligned} -\nabla(\epsilon_w \nabla \Phi) &= q(n_+ - n_-) + qvN_m \\ \epsilon_m &= \epsilon_w \end{aligned} \quad (2.6)$$

Here, ϵ_m is the membrane permittivity. The biomolecule has a variable thickness depending on the number of amino acid attached to the histidine tag with effective dielectric constant same as water. In this chapter, we assume that the effective dielectric constant of the biological membrane is close to water as we are reporting biomolecule sensing in wet environment and charge of the biomolecule is dominant factor here. While in next chapter, we will discuss the prospects of detecting neutral biomolecules based on the dielectric permittivity of the molecule.

(vi) Top oxide-Electrolyte Interface (Detailed Analysis in case for pH sensor): At the electrolyte-top gate oxide interface, the surface of the top oxide is functionalized with surface groups (OH), which protonate and deprotonate as a result of the reactions with protons (H^+) in electrolyte so that the net charge of OH groups respond to the change of pH of the solution. We assume the protonation/deprotonation of OH groups are dictated by the surface binding model. According to the model, the surface chemical reactions that occur on the silicon oxide surface are



Where H_s^+ indicates the protons present nearby the surface. The corresponding equilibrium constants for each reactions can be described by the following equations:

$$\begin{aligned} \frac{[\text{SiOH}][H_s^+]}{[\text{SiOH}_2^+]} &= K_a \\ \frac{[\text{SiO}^-][H_s^+]}{[\text{SiOH}]} &= K_b \end{aligned} \quad (2.8)$$

Where $[H_s^+]$ is the proton concentration at the surface-electrolyte surface. This concentration at the surface can be related to the concentration at the solution bulk by following the Boltzmann distribution such that

$$\begin{aligned} [H_s^+] &= [H_B^+] \exp(-q\Phi_0 / k_B T) \\ \Phi_0 &= \Phi|_{x=0+} - V_{FG} \end{aligned} \quad (2.9)$$

Where $[H_B^+]$ is the proton concentration at the solution bulk and Φ_0 is the electrostatic potential difference between the surface and the electrolyte bulk.

Since the potential of the bulk electrolyte is being held by the bias applied to the fluid gate (FG). The term $[H_B^+]$ in equation is dictated by pH of the electrolyte such that $\text{pH} = -\log_{10} [H_B^+]$.

Now we can express the net charge of surface group per area of the top oxide surface as

$$\sigma_{OH} = q \left([SiOH_2^+] - [SiO^-] \right) \quad (2.10)$$

In addition, the total density of the surface group is

$$N_s = [SiOH] + [SiOH_2^+] + [SiO^-] \quad (2.11)$$

Combining Equations (2.7) - (2.11) results in the expression of σ_{OH} as a function of the potential

$$\sigma_{OH} = qN_s \frac{(10^{-pH} / 10^{-pK_a})e^{-\beta\Phi_0} - (10^{-pK_b} / 10^{-pH})e^{\beta\Phi_0}}{1 + (10^{-pH} / 10^{-pK_a})e^{-\beta\Phi_0} - (10^{-pK_b} / 10^{-pH})e^{\beta\Phi_0}} \quad (2.12)$$

Where $pK_a = -\log_{10} K_a$, $pK_b = -\log_{10} K_b$ and $\beta = q/k_B T$. Thus, the boundary condition at the top oxide-electrolyte interface can be defined

$$(\epsilon_{ox} \nabla \Phi|_{x=0-}) - (\epsilon_m \nabla \Phi|_{x=0+}) = \sigma_{OH} \quad (2.13)$$

The parameters pK_a and pK_b define the affinity of protonation/deprotonation processes of the surface group and here we use the well-known values of pK_a and pK_b in the literature for the SiO_2 [55]

In the native oxide (top and bottom) regions Poisson equation is applied

$$-\nabla \cdot (\epsilon_{ox} \nabla \Phi) = 0 \quad (2.14)$$

With an assumption that the interface traps at the oxide-Si body interfaces (ϵ_{ox} is the permittivity of insulating oxide) are negligible. Finally, the potential at the bottom gate-bottom oxide interface is given by

$$\Phi_{BG-Box} = V_{BG} \quad (2.15)$$

In this model, we have assumed that the sensing device has a planar geometry so that we can solve 1-D Poisson-Boltzmann equations, and for simplicity, the differences of work function between different materials consisting of the DGFET sensors are not considered explicitly.

2.4 Simulator Validation

Equations governing electrostatics in various regions have been listed in Table 2.2 both for pH sensor and potentiometric biosensor. Potential profile along the confinement direction by solving these equations is benchmarked with that of [54] as plotted in Figure 2.3. Drain bias is kept to a small value ($V_{ds}=0.1V$) as conventional for this type of sensor with channel length of $10\ \mu m$ has been used. Therefore, drift diffusion model can be reasonably used for current measurement in these cases. For current simulations, we have used D. Jimenez's current model[56]. Ohmic contacts are assumed for simplicity.

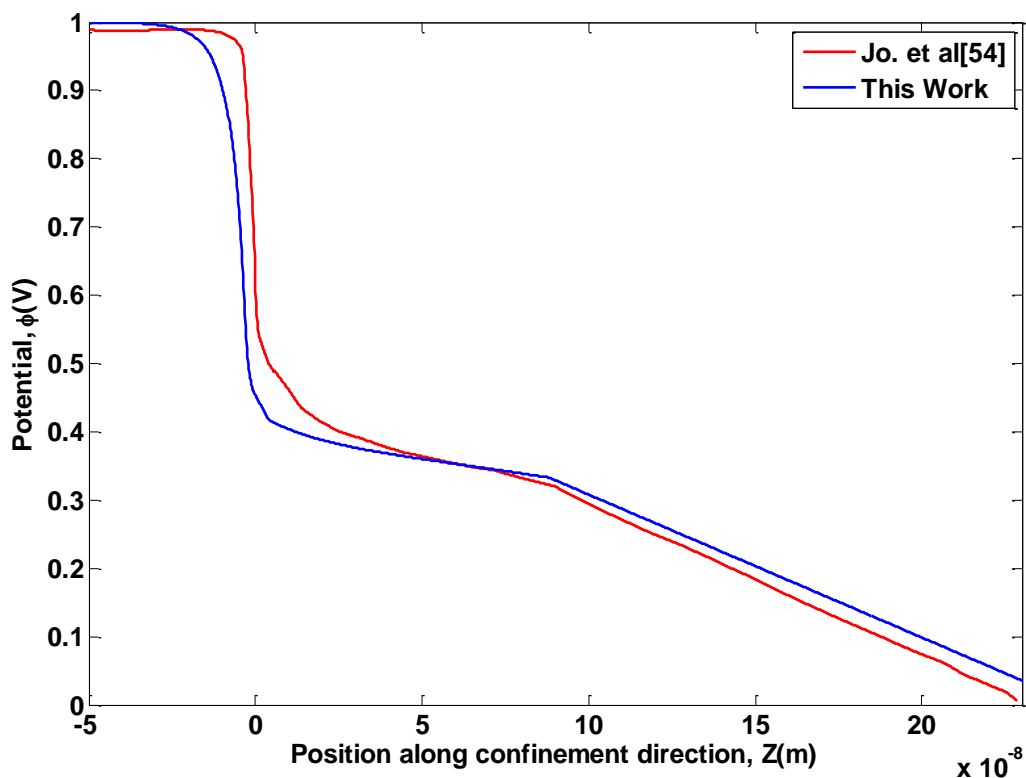


Figure 2.3 Our simulator is benchmarked with that of reported Si pH sensor[54]. Curves indicate the potential profiles associated fluid gate (linear regime, $V_{BG} = 0V$, $V_{FG} = 1V$) operation.

2.5 Current-Voltage modelling of TMDC FET (Drift-Diffusion Region)

For TMDCs transport, classical models will not be appropriate because of the presence of high degree of confinement. The quantum model can be easily formulated by assuming that the potential drop at the ultrathin channel in the confinement direction is negligible. In addition, the potential across the channel can be accurately approximated as a quadratic function of the dimension. Using this approximation and solving Schrödinger and Poisson equation analytically can give the surface potential profile and hence the current transport across the

channel. For modeling threshold voltage only, semi classically approximated charge can be used to obtain simplified closed form equation. Once the primary analytical model is developed, various secondary effects like Mobility Degradation and Interface Traps etc. can be incorporated into the model.

In 2012, Jiménez presented a physics-based model for the surface potential and drain current for monolayer TMDC FET. The work took the 2D density-of-states of the monolayer TMDC and its impact on the quantum capacitance into account and modeled the surface potential. The authors further developed an expression for the drain current considering the drift-diffusion mechanism. The analytical expressions of surface potential and drain current derived in this work are applicable for both the subthreshold and above threshold regions of operation. We have used this model. In 2014, Cao et al[29] presented an analytical I-V model for 2D TMDC FETs as well. The model takes physics of monolayer TMDCs into account and offers a single closed form expression for all three i.e. linear, saturation, and subthreshold regions of operation. The authors also incorporated various non-ideal secondary effects like interface traps, mobility degradation, and inefficient doping in the model, although that resulted in current equations having an integral form instead of closed form.

2.6 Result and Discussion

2.6.1 Application as pH sensor

In this paper, for pH sensor, we have varied top gate oxide and bottom gate oxide thickness for three different TMDC heterostructure FETs separately to find out how sensitivity changes with scaling and material parameter. In DGFET pH sensors, one sweeps the bottom gate (BG) bias, instead of fluid gate (FG), to obtain the transfer characteristics (I_d - V_{BG}) whereas a fixed bias is maintained at the fluid gate, and the corresponding pH sensitivity is measured in terms of the threshold voltage shift. Due to asymmetry of top and bottom oxide thickness, the resultant asymmetry in top and bottom oxide capacitances originates the high pH sensitivity[57] of this sensor according to the following equation:

$$\frac{\Delta V_{BG}}{\Delta pH} = \alpha_{SN} \left(\frac{C_{tox}}{C_{box}} \right) \left(\frac{\Delta V_{FG}}{\Delta pH} \right) \quad (2.16)$$

In this work, we have used high gate bias for front gate ($V_{FG} = 1V$) for all the pH sensor and biosensor performance evaluation. So, α_{SN} will be close to one [57][58][59] for this work. That is why back gate threshold voltage will vary approximately linearly with the change of

pH considering that $\left(\frac{\Delta V_{FG}}{\Delta pH}\right)$ will be less than the Nernst limit and be almost constant during the sweep of back gate voltage. Approximately identical super-Nernst sensitivity is obtained for all trilayer FETs for a wide range of operation [pH 4 to 8] for various back oxide thicknesses as seen from Figure 2.10. Another point to note from Figure 2.10 is that sensitivity increases almost linearly with the increase of back oxide thickness while keeping front oxide thickness fixed at 2 nm. Figure 2.4 to Figure 2.9 support the claim as evident from the extension of the spread of drain current in sub threshold region with the increase of back oxide thickness. This is also consistent with equation 2.15. Increase of T_{BOX} will reduce C_{box} and ultimately increases the sensitivity. However, it must be mentioned that the sensitivity reported in this work will be an upper level estimation of not yet experimentally measured sensitivity because of the assumptions made in section 2.4.

Increase of spread of drain current for pH 4 to 8 in sub threshold region with the increase of back oxide thickness for every trilayer material channel FETs results in shift in threshold voltage, $\Delta V_{T, BG}$ as shown in Figure 2.5, Figure 2.7 and Figure 2.9.

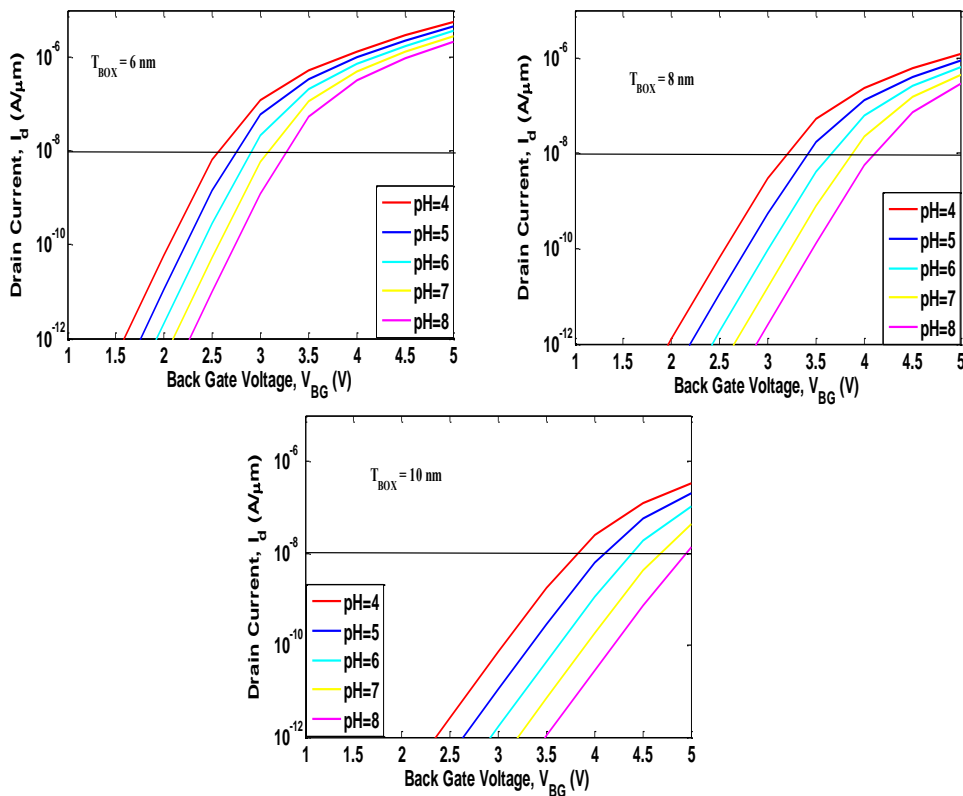


Figure 2.4 depicts the increase of the difference of V_T for various pH with the increase of bottom oxide thickness and provides insights towards the upward movement of the ΔV_T for various thicknesses. This figure is for $\text{MoS}_2/\text{WS}_2/\text{MoS}_2$ FET pH sensor. Here, $V_{FG} = 1$ V.

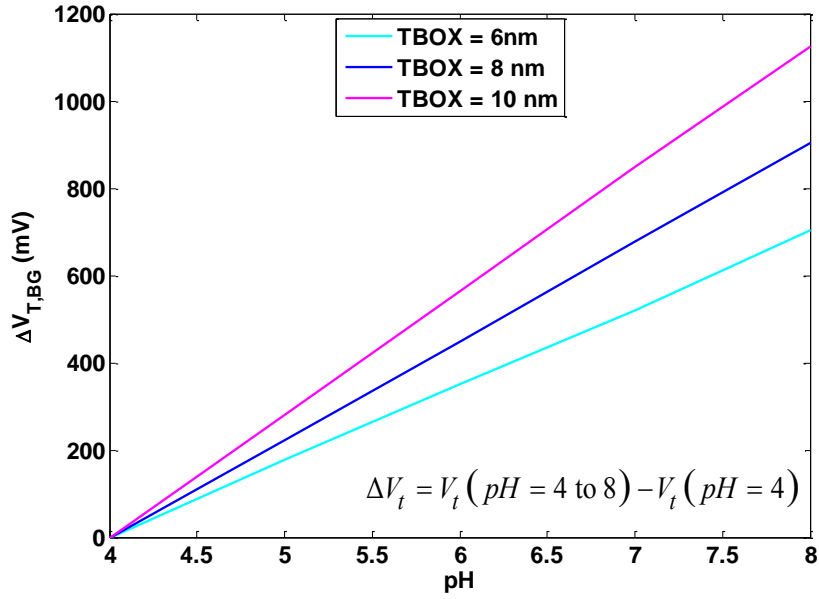


Figure 2.5 Figure shows shift of V_T with pH for back gate operation, which is above the Nernst limit (MoS₂/WS₂/MoS₂ FET pH sensor). The linearity of the curves can be traced to the equation 2.15.

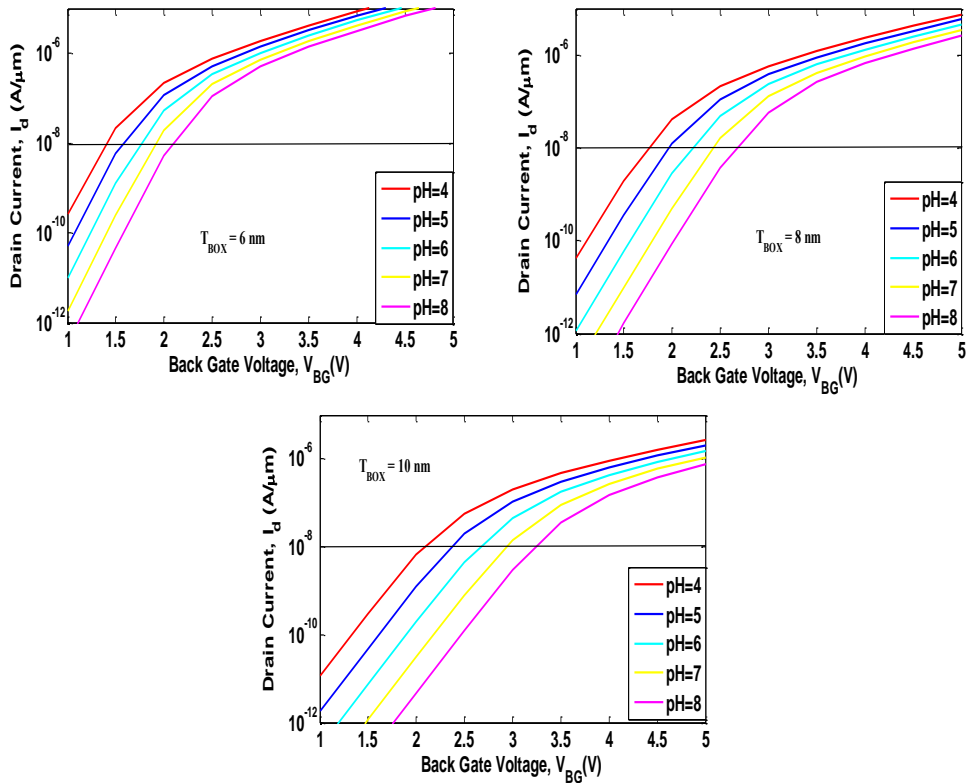


Figure 2.6 depicts the increase of the difference of V_T for various pH with the increase of bottom oxide thickness and provides insights towards the upward movement of the ΔV_T for various thicknesses. This figure is for MoS₂/MoSe₂/MoS₂ FET pH sensor. Here, $V_{FG} = 1V$.

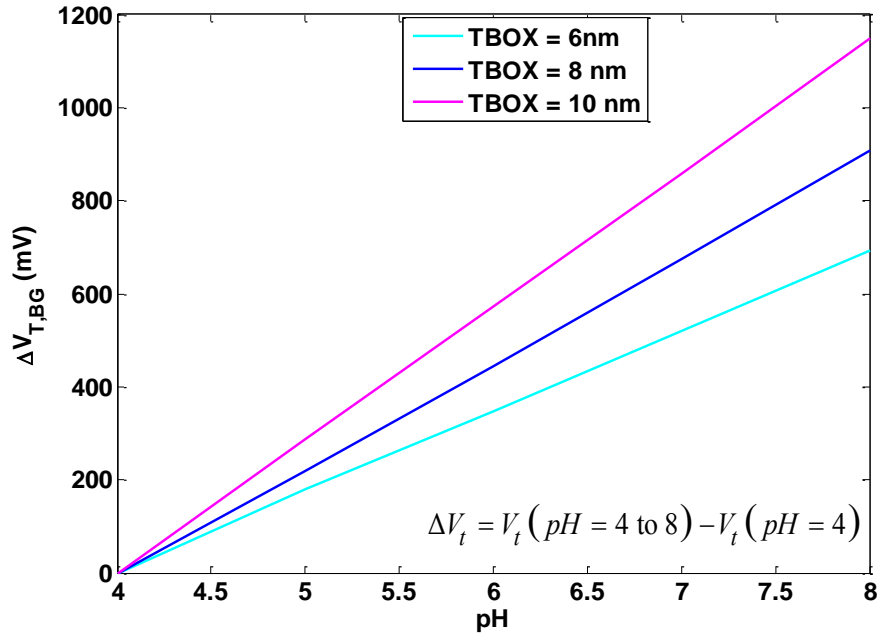


Figure 2.7 Figure shows shift of V_T with pH for back gate operation, which is above the Nernst limit ($\text{MoS}_2/\text{MoSe}_2/\text{MoS}_2$ FET pH sensor). The linearity of the curves can be traced to the equation 2.15.

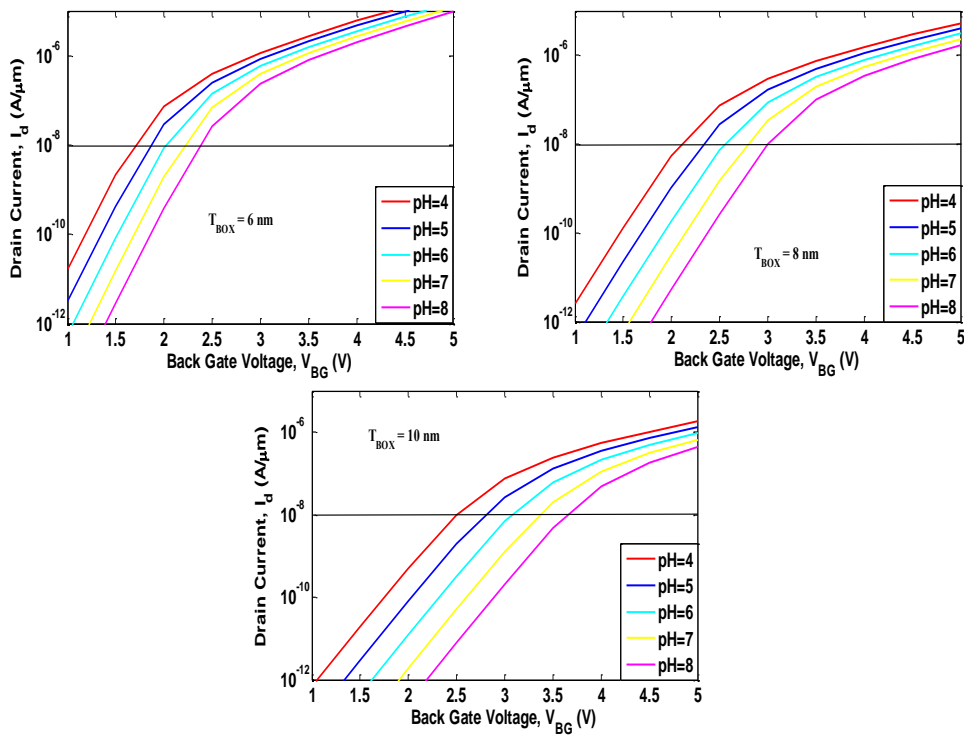


Figure 2.8 depicts the increase of the difference of V_T for various pH with the increase of bottom oxide thickness and provides insights towards the upward movement of the ΔV_T for various thicknesses. This figure is for $\text{MoS}_2/\text{WSe}_2/\text{MoS}_2$ pH sensor. Here, $V_{FG} = 1\text{V}$.

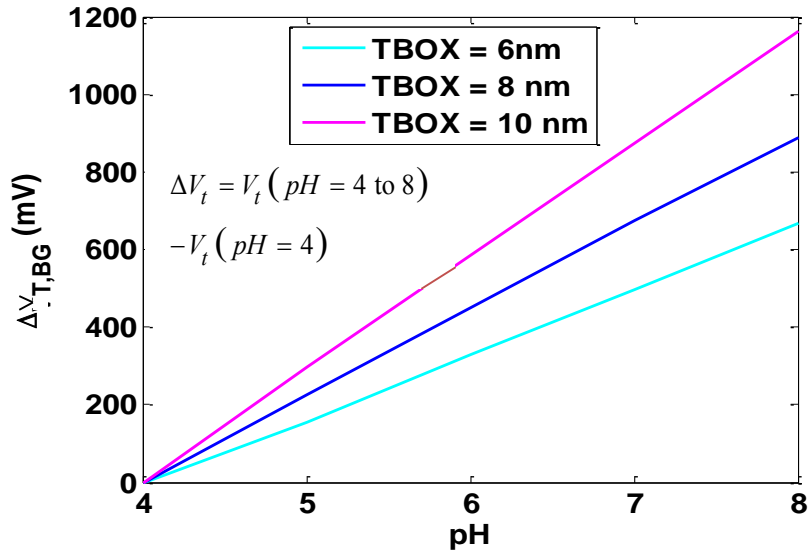


Figure 2.9 Figure shows shift of V_T with pH for back gate operation, which is above the Nernst limit ($\text{MoS}_2/\text{WSe}_2/\text{MoS}_2$ FET pH sensor). The linearity of the curves can be traced to the equation 2.15.

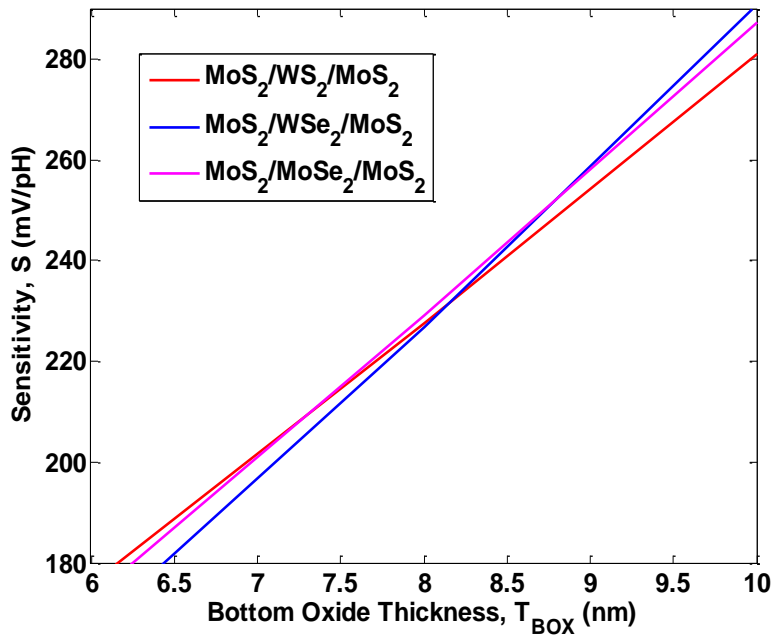


Figure 2.10 Sensitivity v/s Bottom oxide thickness for all these trilayer TMDC FET pH sensors.

It is evident from the equation 2.16 and Figure 2.13 that increasing the top oxide thickness results in a reduction of sensitivity while the opposite trend is observed for bottom oxide. As evident from equation 2.16, an increase in T_{TOP} will reduce C_{tox} ultimately decreasing the sensitivity. This finding is also consistent with the trend found in literature[54].

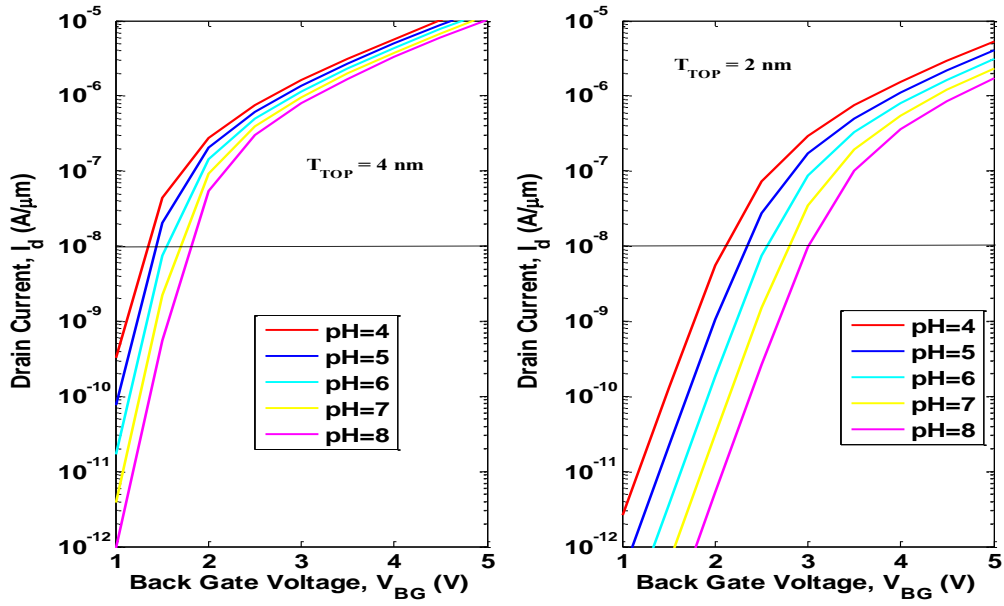


Figure 2.11 shows the narrowing of drain current in the sub threshold region with the increase of top oxide thickness. This figure is for MoS₂/WSe₂/MoS₂ pH sensor. Here, V_{FG} = 1V.

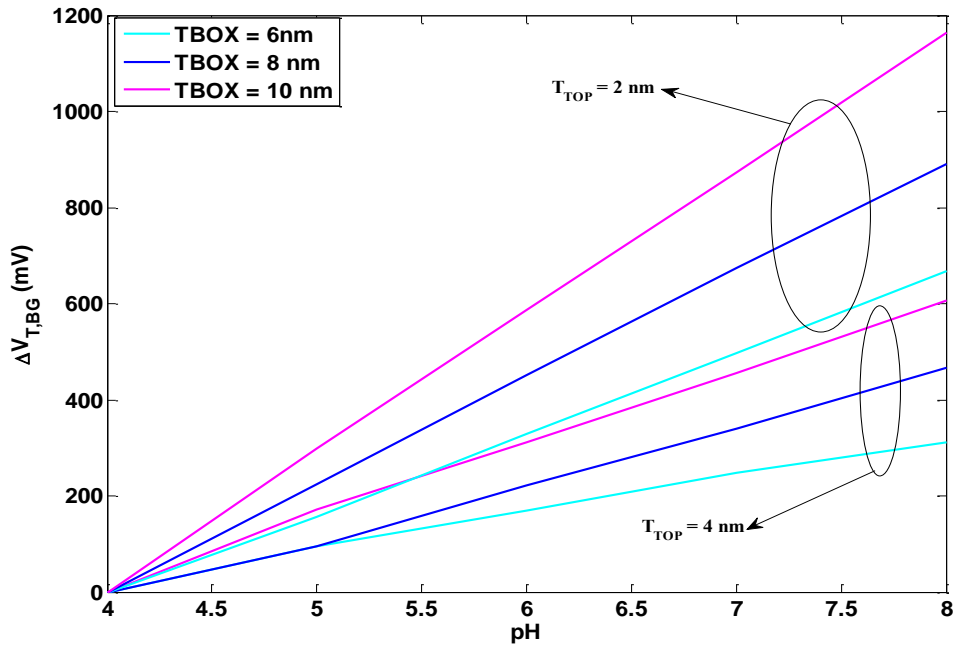


Figure 2.12 depict the sensitivity of MoS₂/WSe₂/MoS₂ TMD FET pH sensor for top oxide scaling.

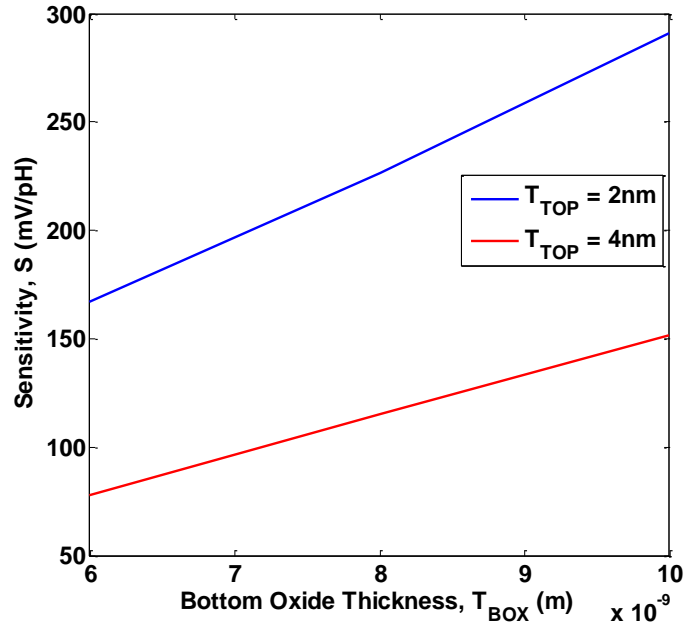


Figure 2.13 pH sensitivity for different bottom oxide thickness with top oxide thickness as a parameter for MoS₂/WSe₂/MoS₂ trilayer ISFET. Increasing top oxide thickness reduces sensitivity and we get opposite trend for bottom oxide.

Since the trend is similar for all three trilayer FETs, we have shown output for only MoS₂/WSe₂/MoS₂ DGFET pH sensor.

2.6.2 Application as Biosensor

To evaluate the prospect of these materials in a FET based Nano biosensor, we have considered more realistic structure of Figure 2.2 (right). We have varied the no. of aspartic acid charges to find out the sensitivity of these sensors. Sensitivity in the case of biosensor is defined as the ratio of the difference in current before and after biomolecule binding to the lower of the two currents[41]. The magnitude of the negative protein charge density increases with the number of aspartic acids.

This results in a lower potential in the charged part of the protein region. As a result, surface potential (potential at top gate oxide-receptor interface) decreases with increasing protein charge. This potential acts as top gate voltage in current simulator. Since surface potential is decreasing with the increasing no. of aspartic acid, current will decrease for all three devices as seen from Figure 2.14.

From Figure 2.15, which is obtained from Figure 2.14, it is noticeable that, all three FETs show highest sensitivity (approximately 10^5 or above) in the subthreshold region. Among all these three FETs, MoS₂/WS₂/MoS₂ FET shows the lowest sensitivity for wide region of operation. The observed trend of high sensitivity in subthreshold region is quite similar to that of experimentally reported Silicon FET [60] as well as multilayer MoS₂ based biosensors [41][44].

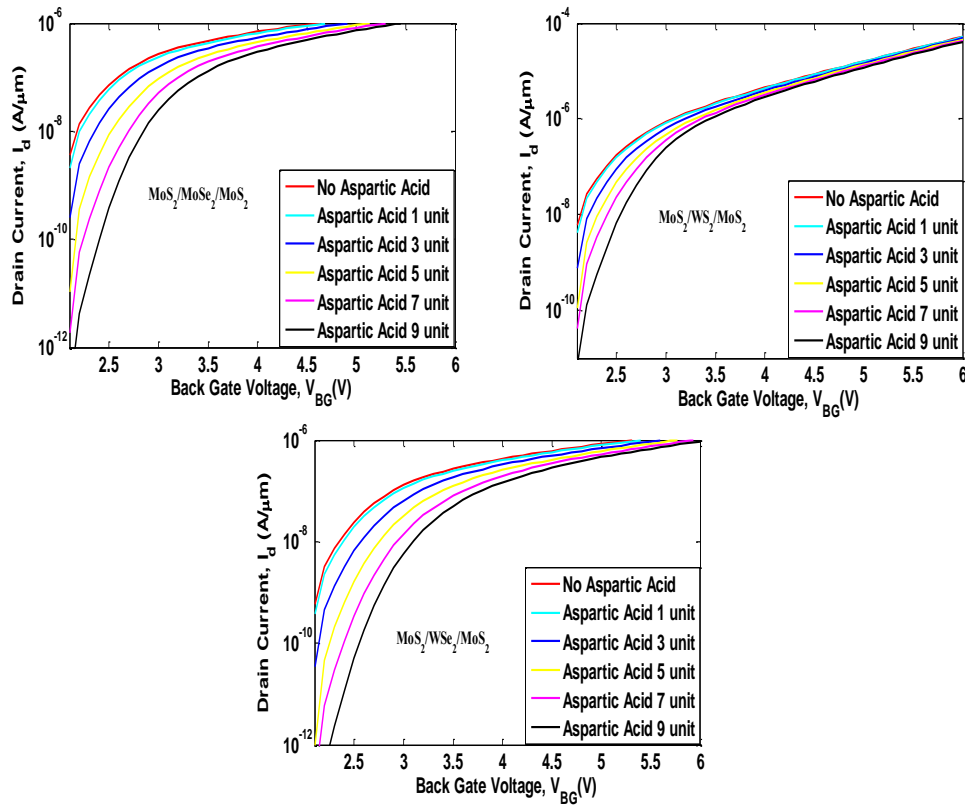


Figure 2.14 I_d - V_{BG} characteristics of different-trilayer TMDC heterostructure biosensors for different no of Aspartic acids. Spread of the drain current in the subthreshold region is the lowest for MoS₂/WS₂/MoS₂ trilayer DGFET biosensor for various no. of Aspartic acids among these three FETs. For these three heterostructure FETs, no significant difference in device current is observed for various acids in ‘on’ region resulting in a low sensitivity for all of them in ‘on’ condition. Here, V_{FG} is considered 1V.

As seen from the Figure 2.14, the relative change in transistor on current with the increasing no of aspartic acid is relatively small compared to that in subthreshold regime. This is because the FET is already conducting a high current in ‘on’ condition, so a small change in surface potential due to the attachment of a biomolecule results in a corresponding small change in the drain current. However, in completely off device or in subthreshold regime, FET conducts little or no current. Therefore, a small change in surface potential due to binding of protein brings relatively larger change in drain current. This phenomenon can be explained from another viewpoint. In the subthreshold region, the drain current has exponential dependence on the gate

dielectric surface potential, while in saturation and linear regions the relationship is quadratic and linear, respectively. Hence, the sensitivity in the subthreshold region is much higher compared to those in the saturation and linear regions. These findings indicate that biosensor operation in subthreshold regime will optimize the sensor response for these heterostructure FETs while improving the lower limit of bio molecule detection at the same time.

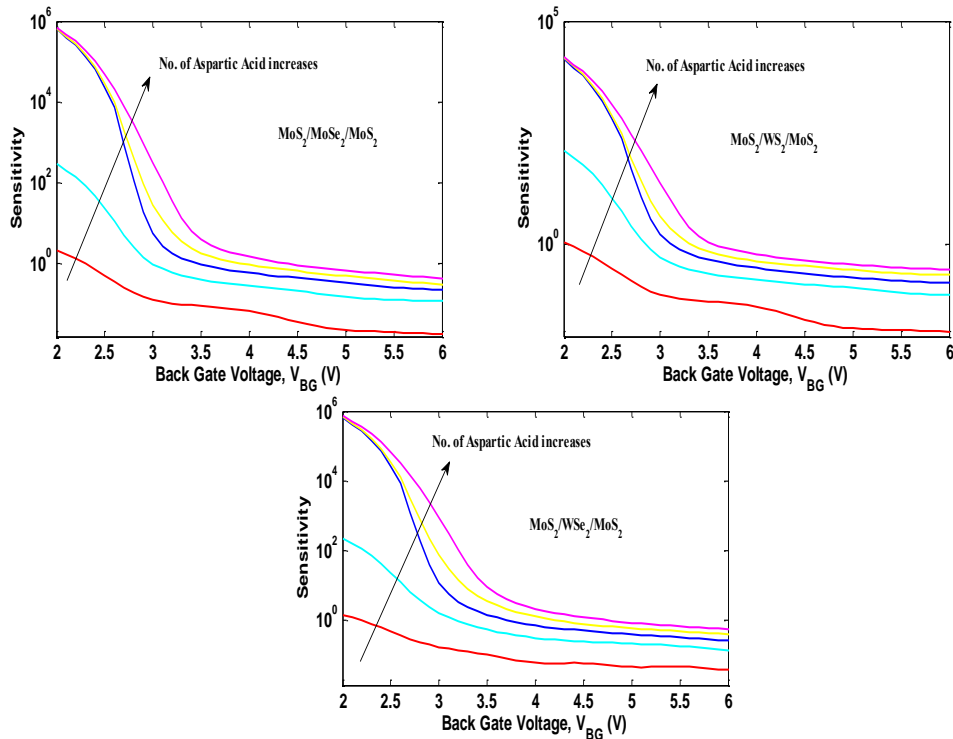


Figure 2.15 Current sensitivity of different-trilayer TMDC heterostructure biosensors for various no. of Aspartic acid as a function of back gate voltage. Here sensitivity is defined as a ratio of currents. Therefore, sensitivity is unit less for biosensor unlike pH sensor. Highest sensitivity is found in subthreshold region for all three FETs. $\text{MoS}_2/\text{WSe}_2/\text{MoS}_2$ and $\text{MoS}_2/\text{MoSe}_2/\text{MoS}_2$ FET show similar sensitivity for wide range of gate voltages while $\text{MoS}_2/\text{WS}_2/\text{MoS}_2$ FET shows least sensitivity among them, notably in subthreshold region.

Chapter 3

Analytical Modeling of Dielectric Modulated Double Gate Junctionless MOSFET

3.1 Introduction

Currently available technology for detecting tumor markers, antigen-antibody complexes, and pathogens is time-consuming, complex, and expensive[61], [62]. FET based biosensors have emerged as potential candidate in label free detection of biomolecules like cancer biomarkers, Protein, DNA and other pathogens in a cost effective and reliable alternative to optical detection technique. The first concept of electronic pH sensing with ion-sensitive field effect transistors (ISFETs) was suggested by Bergveld [8]. The pH sensitivity (mV/pH) of a conventional single-gated ISFET is defined by the changes of threshold voltage (V_T) at a given amount of pH changes. However, such sensitivity is limited to Nernst limit of 59 mV/pH. To overcome the Nernst limit of sensitivity in single-gated ISFET recent literatures [54], [57] have suggested double-gated field effect transistors.

A modified version of ISFETs have also been used to detect biomolecules like DNA, Protein and biomarkers indicative of various diseases. However, there are several problems in detecting biomolecule reliably using ISFET. First of all, the electrical signals from the ISFET biosensor depends on the ionic concentration of the sample solution[63] which is characterized by Debye length. Second, various ionic concentrations of the sample can significantly change the electrical signal of ISFET biosensors [64]. Third, controlling the ionic concentration accurately of any real human sample, such as blood serum, urine or saliva is difficult[65]. Moreover, the conductance modulation in the FET sensor is caused by the interaction potential and this potential might be partially screened by the strong ionic strength of the buffer solution. This screening directly depends on the Debye–Hückel length[65]. Therefore, Debye-screening-free sensors working under the dry environment can provide several advantages over electrolyte-based biosensors. In the present work, Junctionless Double Gate(JL-DG) MOSFET under dry environment condition[66] has been investigated for its application as a biosensor for the label free electrical detection of the biomolecules. Fabrication feasibility of Nanowire Junctionless MOSFET (JL-MOSFETs) have been already demonstrated by Colinge et al. [67][68].

Immunity to various Short Channel Effects (SCEs) like DIBL, improved on state and transfer characteristics have made JL-MOSFETS more advantageous over their conventional counterparts like junction based FETs[69], [70]. Therefore, JL-DG MOSFET with cavity regions functionalized for detecting biomolecule in dry environment can be a viable solution to the problems associated with biomolecule sensing under aqueous electrolyte condition. In dielectric modulated field-effect transistor (DM-FET), insulator layer is etched to create a nanogap region underneath the gate material. DM-FET is capable of detecting even neutral biomolecules that is not possible with conventional ISFET based biosensor. DM-FET based sensor also shows great compatibility with standard CMOS process[47], [71], [72]. In our work, we have extended the model widely used in literature[66], [73]–[77] to four regions in place of three regions namely cavity, oxide and cavity again. It has been demonstrated experimentally that even under the precisely controlled experiments, the complete fill-in is difficult to achieve[78]. Along with the fill-in factor, the possible location of biomolecule binding site within the nanogap (cavity) can differ. Therefore, it should be analyzed. In practical situation, the capture of biomolecules can be asymmetric and random and quite complex due to low binding probability in a carved nanogap [72]. Therefore, the study of biosensor with partially filled and randomly distributed biomolecule can provide valuable insight to the dependence of sensitivity on biomolecule position and percentage fill in of nanogap cavity region. Though the modelling scheme has been used already in literature, four-region MOSFET sensor with focus on finding the optimum position of biomolecule has not been reported yet. We have effectively captured the drain bias effect on sensor's performance also by interchanging the drain-source regions of the sensor.

3.2 Device Structure

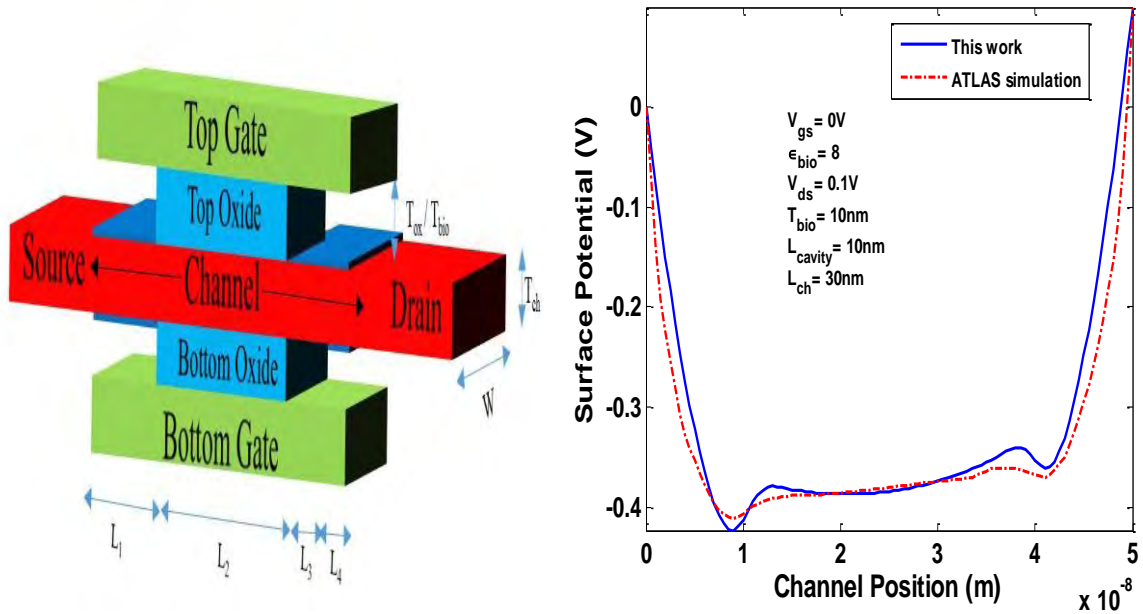


Figure 3.1 (Left) Schematic initial structure of Junctionless DM-DG-MOSFET biosensor. Different parameters considered here are as follows, $T_{bio}/T_{ox} = 9$ nm with 1 nm Native SiO_2 , $T_{ch} = 10$ nm, $L_1=10$ nm, $L_2=30$ nm, $L_3=L_4=5$ nm. Doping in source, drain and channel is $1 \times 10^{25} \text{ m}^{-3}$. (Right) (b) Comparison of surface potential obtained from analytical model and ATLAS simulation for the device in left.

The device architecture for n-type Junctionless Dielectric Modulated Double Gate MOSFET based biosensors used in this work is depicted in Figure 3.1. Here, L_1 , L_3 and L_4 are the length of the nanogap cavity; L_2 is the length of the gate oxide SiO_2 . T_{bio} , T_{ch} , T_{ox} are the thickness of the nanogap cavity, channel and gate oxide respectively. For initial structure the typical values of different parameters used here are $T_{bio}/T_{ox} = 9$ nm, $T_{ch} = 10$ nm, $L_1=10$ nm, $L_2=30$ nm, $L_3=L_4=5$ nm. Adhesion layer is used for the immobilization of biomolecules. These nanogap cavity regions serve as sensing sites, in which the target biomolecules are immobilized. The results from analytical modeling were verified by simulation results from ‘Silvaco Atlas’, which is commonly used to characterize the electrical properties of the semiconductor devices[79]. The presence of the neutral biomolecules in the nanogap cavity is simulated by introducing material having dielectric constant ($\epsilon_{bio} > 1$) corresponding to biomolecules (for e.g. streptavidin = 2.1[80], protein = 2.50, biotin = 2.63[81], and APTES = 3.57 [82], [83]) in the nanogap cavities. In order to simulate the effect of charged biomolecules, negative or positive interface fixed charge ($N_f = \pm 3 \times 10^{16} \text{ m}^{-2}$) (for e.g. DNA) at the SiO_2 -Air interface of the device can be considered in this model. Quantum effects have not been considered in the simulation and model to reduce the computational burden while maintain significant accuracy. Before biomolecule immobilization, the underlap region is empty and thus filled with air

(dielectric constant $\epsilon_{air} = 1$). To simulate the presence of biomolecules in the nanogap cavity region, an oxide layer with height of $T_{bio} = 9$ nm is defined and its dielectric constant is varied as $\epsilon_{bio} = 2, 3, 4, 5, 7$. The height/thickness of the layer is so chosen to resemble the varying height of the biomolecules[77] [79].

3.3 Working principle of the device

The nanogap cavity regions formed in the gate oxide of the device serve as sensing sites in which the target biomolecules are immobilized. When the target biomolecules are absent in the nanogap cavity region, it means the cavities are filled with air, so dielectric constant of the cavity region is different from that of region II and the threshold voltage changes with respect to its initial values. When target biomolecules (like Streptavidin, Biotin, Avidin, enzyme, cell, DNA, APTES) are present and immobilized at the binding site, the dielectric constant changes and the gate capacitance of the device also changes. Consequently, electrical characteristics of the device, such as threshold voltage changes according to the dielectric constant or charge of the target biomolecules.

3.4 Analytical Model Development

To obtain analytical expression for potential distribution and drain current, the channel is divided in to four regions as follows:

$$\text{Region I:} \quad 0 \leq x \leq t_{si}, 0 \leq y \leq L_1 \quad (3.1)$$

$$\text{Region II:} \quad 0 \leq x \leq t_{si}, L_1 \leq y \leq L_1 + L_2 \quad (3.2)$$

$$\text{Region III:} \quad 0 \leq x \leq t_{si}, L_1 + L_2 \leq y \leq L_1 + L_2 + L_3 \quad (3.3)$$

$$\text{Region IV:} \quad 0 \leq x \leq t_{si}, L_1 + L_2 + L_3 \leq y \leq L_1 + L_2 + L_3 + L_4 \quad (3.4)$$

Potential distribution is obtained by solving the Poisson's equation separately in each region as follows:

$$\frac{\partial^2 \phi_i(x, y)}{\partial x^2} + \frac{\partial^2 \phi_i(x, y)}{\partial y^2} = \frac{qN_a}{\epsilon_{si}} \quad \text{For p-type JL DM DG MOSFET} \quad (3.5)$$

$$\frac{\partial^2 \phi_i(x, y)}{\partial x^2} + \frac{\partial^2 \phi_i(x, y)}{\partial y^2} = -\frac{qN_d}{\epsilon_{si}} \quad \text{For n-type JL DM DG MOSFET} \quad (3.6)$$

Where $i = 1, 2, 3, 4$ for region 1, 2, 3 and 4, respectively. $\phi_i(x, y)$ is the 2-D potential distribution in the Silicon channel, N_a and N_d are the doping in the silicon channel, q is the electron charge, and ϵ_{si} is the dielectric permittivity of Silicon. Using parabolic approximation[84], $\phi_i(x, y)$ is given by

$$\phi_i(x, y) = P_{0i}(y) + P_{1i}(y)x + P_{2i}(y)x^2 \quad (3.7)$$

Where $P_{0i}(y)$, $P_{1i}(y)$, and $P_{2i}(y)$ are coefficients and obtained by using following boundary conditions. Equations 3.11 and 3.13 are inward and outward fluxes resulted from gauss law.

$$\phi_i(0, y) = \phi_{fsi}(y) \quad (3.8)$$

$$\phi_i(t_{si}, y) = \phi_{bsi}(y) \quad (3.9)$$

$$\phi_i\left(\frac{t_{si}}{2}, y\right) = \phi_{ci}(y) \quad (3.10)$$

$$\frac{\delta \phi_i(0, y)}{\delta x} = \frac{C_i}{\epsilon_{si}} (\phi_{fsi}(y) - V_{gs} + V_{fbi}) \quad (3.11)$$

$$\frac{\delta \phi_i\left(\frac{t_{si}}{2}, 0\right)}{\delta x} = 0 \quad (3.12)$$

$$\frac{\delta \phi_i(t_{si}, y)}{\delta x} = -\frac{C_i}{\epsilon_{si}} (\phi_{bsi}(y) - V_{gs} + V_{fbi}) \quad (3.13)$$

$\phi_{fsi}(y)$ is the front gate surface potential and $\phi_{bsi}(y)$ is the back gate surface potential, $\phi_{ci}(y)$ is the central potential, V_{gs} is the gate to source voltage and V_{fbi} is the flat band voltage, which is given by

$$V_{fb2} = \phi_m - \phi_{si} \quad (3.14)$$

$$\phi_{si} = \chi_{si} + \frac{E_g}{2} \quad (3.15)$$

$$V_{fb1} = V_{fb3} = V_{fb4} = V_{fb2} - \frac{qN_f}{C_{gap}} \quad (3.16)$$

$$C_{gap} = \frac{\epsilon_{bio}}{t_{bio}} \quad (\text{Effective capacitance of cavity regions}) \quad (3.17)$$

C_i is the gate capacitance per unit area of the gate dielectric of JL-DM-DG-MOSFET.

$$C_1 = C_3 = C_4 = C_{eff} \quad \text{Assuming all three regions contain biomolecule} \quad (3.18)$$

Where

$$C_{eff} = \frac{\epsilon_{bio}\epsilon_{ox1}}{\epsilon_{bio}t_{ox1} + \epsilon_{ox1}t_{bio}} \quad (3.19)$$

$$C_2 = C_{ox} \quad (3.20)$$

$$C_{ox} = \frac{\epsilon_{ox}}{t_{ox}} \quad (3.21)$$

Where N_f the charge density (m^{-2}) of biomolecules, ϵ_{bio} is the permittivity of the biomolecules present in cavity and ϵ_{ox1} is the permittivity of the SiO_2 layer. Substituting constants $P_{0i}(y)$, $P_{1i}(y)$ and $P_{2i}(y)$ value in Eq. (3.7) to obtain surface potential

$$P_{0i}(y) = \phi_{fsi}(y) \quad (3.22)$$

$$P_{1i}(y) = \frac{C_i}{\epsilon_{si}}(\phi_{fsi}(y) - V_{gs} + V_{fbi}) \quad (3.23)$$

$$P_{2i}(y) = -\frac{C_i}{\epsilon_{si}t_{si}}(\phi_{fsi}(y) - V_{gs} + V_{fbi}) \quad (3.24)$$

$$\phi_i(x, y) = \phi_{fsi}(y) + \frac{C_i}{\epsilon_{si}}(\phi_{fsi}(y) - V_{gs} + V_{fbi})x - \frac{C_i}{\epsilon_{si}t_{si}}(\phi_{fsi}(y) - V_{gs} + V_{fbi})x^2 \quad (3.25)$$

Since $\varphi_{ci}(y)$ should be relevant to the punch through current, we obtained the relation between $\varphi_{fsi}(y)$ and $\varphi_{ci}(y)$ from (above equation) by substituting $x = t_{si}/2$. Hence, we obtain

$$\varphi_i(x, y) = \frac{1}{1 + \frac{C_i t_{si}}{4\epsilon_{si}}} \left[\varphi_{ci}(y) + \frac{C_i t_{si}}{4\epsilon_{si}} (V_{gs} - V_{fbi}) \right] \left(1 + \frac{C_i}{\epsilon_{si}} x - \frac{C_i}{\epsilon_{si} t_{si}} x^2 \right) \quad (3.26)$$

$$- \frac{C_i}{\epsilon_{si}} x (V_{gs} - V_{fbi}) + \frac{C_i}{\epsilon_{si} t_{si}} x^2 (V_{gs} - V_{fbi})$$

Where

$$\varphi_{fsi}(y) = \frac{1}{1 + \frac{C_i t_{si}}{4\epsilon_{si}}} \left[\varphi_{ci}(y) + \frac{C_i t_{si}}{4\epsilon_{si}} (V_{gs} - V_{fbi}) \right]$$

Putting 3.26 into 3.1 and then rearranging we get

$$\frac{\delta\varphi_{ci}(y)}{\delta y^2} - \frac{\varphi_{ci}(y) - V_{gs} + V_{fbi}}{\eta_i^2} = -\frac{qN_d}{\epsilon_{si}} \quad (3.27)$$

Where

$$\frac{1}{\eta_i^2} = \frac{8C_i}{4\epsilon_{si} t_{si} + C_i t_{si}^2} \quad (3.28)$$

Solving Eq. 3.27, we get

$$\varphi_{ci}(y) = A_i e^{\frac{y}{\eta_i}} + B_i e^{-\frac{y}{\eta_i}} + \sigma_i \quad (3.29)$$

$$\sigma_i = -\eta_i^2 \frac{qN_d}{\epsilon_{si}} - (V_{gs} - V_{fbi}) \quad \text{For n-type JL DM DG MOSFET} \quad (3.30)$$

Constant A_i and B_i are obtained by using the boundary conditions at the source and drain junctions such as

$$\varphi_{ci}(0) = V_{bi} \quad (3.31)$$

$$\varphi_{ci}(L_1 + L_2 + L_3 + L_4) = V_{bi} + V_{ds} \quad (3.32)$$

$$V_{bi} = 0 \quad (3.33)$$

Solving boundary conditions, we get

$$B_1 = \frac{(V_{bi} - \sigma_1)e^{\frac{L_1}{\eta_1}} - (\psi_1 - \sigma_1)}{2 \sinh(\frac{L_1}{\eta_1})} \quad (3.34)$$

$$A_1 = V_{bi} - \sigma_1 - B_1 \quad (3.35)$$

$$B_2 = \frac{(\psi_1 - \sigma_2)e^{\frac{L_2}{\eta_2}} - (\psi_2 - \sigma_2)}{2 \sinh(\frac{L_2}{\eta_2})e^{-\frac{L_1}{\eta_2}}} \quad (3.36)$$

$$A_2 = \frac{\psi_1 - \sigma_2 - B_2e^{-\frac{L_1}{\eta_2}}}{e^{\frac{L_1}{\eta_2}}} \quad (3.37)$$

$$B_3 = \frac{(\psi_2 - \sigma_3)e^{\frac{L_3}{\eta_3}} - (\psi_3 - \sigma_3)}{2 \sinh(\frac{L_3}{\eta_3})e^{-\frac{(L_1+L_2)}{\eta_3}}} \quad (3.38)$$

$$A_3 = \frac{\psi_2 - \sigma_3 - B_3e^{-\frac{(L_1+L_2)}{\eta_3}}}{e^{\frac{(L_1+L_2)}{\eta_3}}} \quad (3.39)$$

$$B_4 = \frac{(\psi_3 - \sigma_4)e^{\frac{L_4}{\eta_4}} - (V_{bi} + V_{ds} - \sigma_4)}{2 \sinh(\frac{L_4}{\eta_4})e^{-\frac{(L_1+L_2+L_3)}{\eta_4}}} \quad (3.40)$$

$$A_4 = \frac{\psi_3 - \sigma_4 - B_4e^{-\frac{(L_1+L_2+L_3)}{\eta_4}}}{e^{\frac{(L_1+L_2+L_3)}{\eta_4}}} \quad (3.41)$$

V_{bi} is the built-in potential, ψ_1 , ψ_2 and ψ_3 are the intermediate potentials, obtained by maintaining continuity of the potential and lateral electric field at the interface of each region.

Calculation of ψ_1 , ψ_2 and ψ_3 is explained in detail in Appendix A.

Continuous surface potential for complete channel length can be obtained from Eq. (3.7).

$$\phi_1(x, y) = P_{01}(y) + P_{11}(y)x + P_{21}(y)x^2 \quad (3.42)$$

$$\phi_2(x, y) = P_{02}(y) + P_{12}(y)x + P_{22}(y)x^2 \quad (3.43)$$

$$\phi_3(x, y) = P_{03}(y) + P_{13}(y)x + P_{23}(y)x^2 \quad (3.44)$$

$$\phi_4(x, y) = P_{04}(y) + P_{14}(y)x + P_{24}(y)x^2 \quad (3.45)$$

Drain current in the subthreshold region is obtained by using the expression of potential (Eq. (3.42~3.45)), and is given by

$$I_{dsub} = \frac{W \mu k T (1 - \exp(-\frac{V_{ds} q}{k T}))}{\left(\int_0^{L_1} \frac{1}{\int_0^{t_{si}} n_i \exp(\frac{\phi_1(x, y) q}{k T}) dx} dy + \int_0^{L_2} \frac{1}{\int_0^{t_{si}} n_i \exp(\frac{\phi_2(x, y) q}{k T}) dx} dy \right.} \quad (3.46)$$

$$\left. + \int_0^{L_3} \frac{1}{\int_0^{t_{si}} n_i \exp(\frac{\phi_3(x, y) q}{k T}) dx} dy + \int_0^{L_4} \frac{1}{\int_0^{t_{si}} n_i \exp(\frac{\phi_4(x, y) q}{k T}) dx} dy \right)$$

Here, n_i is the intrinsic carrier concentration and μ is the carrier mobility.

3.5 Results and Discussions

3.5.1 Variation of Sensitivity with Position of Biomolecule

We have investigated the effect of biomolecule position on threshold voltage of the device to find out sensitivity to detect biomolecule. We have used Figure 3.1 where it is possible to fill the cavity region partially with biomolecule while the region left is to be filled with air. Actually, such an arrangement of biomolecules can offer a good insight to effect of percentage area coverage of biomolecule on device sensitivity. We also vary the position of partially filled biomolecule to determine whether such variations yield a better sensitivity or not. To investigate those critical effects of biomolecule position and Fill in factor in cavity region on sensitivity, we have divided the total oxide layer in to 4 separate regions as mentioned in Eq. (3.1-3.4). In this study, we have set the dimensions of those four regions as $L_1=10nm$, $L_2=30nm$, $L_3=5nm$ and $L_4=5nm$. Region II ($L_2=30nm$) is kept as a fixed oxide layer whereas Region I, III and IV work as cavity for biomolecule placement. These three regions can be either filled with biomolecules or kept empty. This will result in different possible cases based on the presence or absence of biomolecule. Moreover, based on whether Region I or Region IV is connected to the drain, each variation of position of biomolecule will result into two different configuration of biomolecule's distribution in the cavity sites. Here we define sensitivity as

$$\Delta V_{th} = V_{th}(\epsilon_{bio}) - V_{th}(\epsilon_{air})$$

3.5.2 Dependence of Sensitivity on Biomolecule's Position when Region IV is connected to Drain

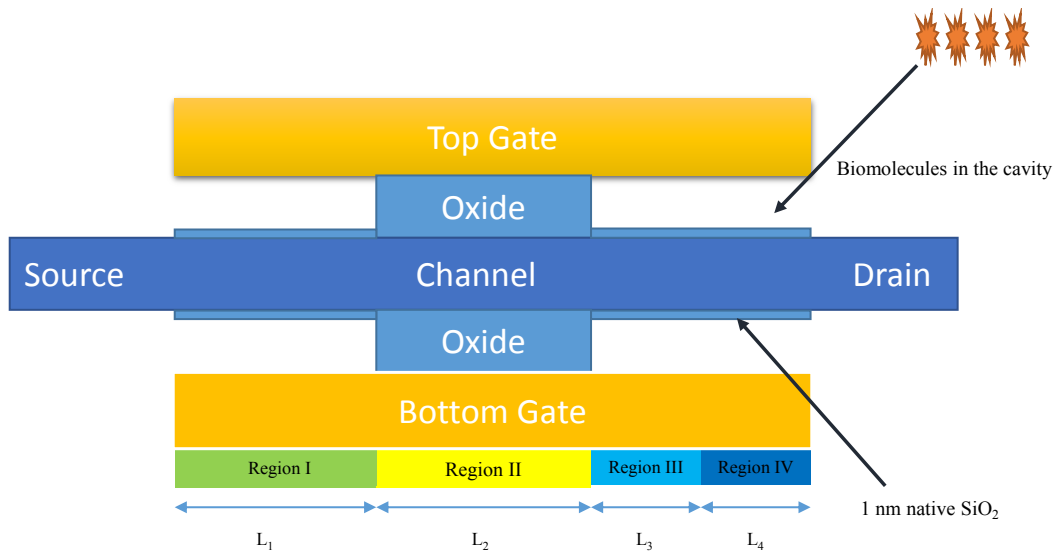


Figure 3.2 2D view (side) of Figure 3.1. Here Region IV is connected to drain.

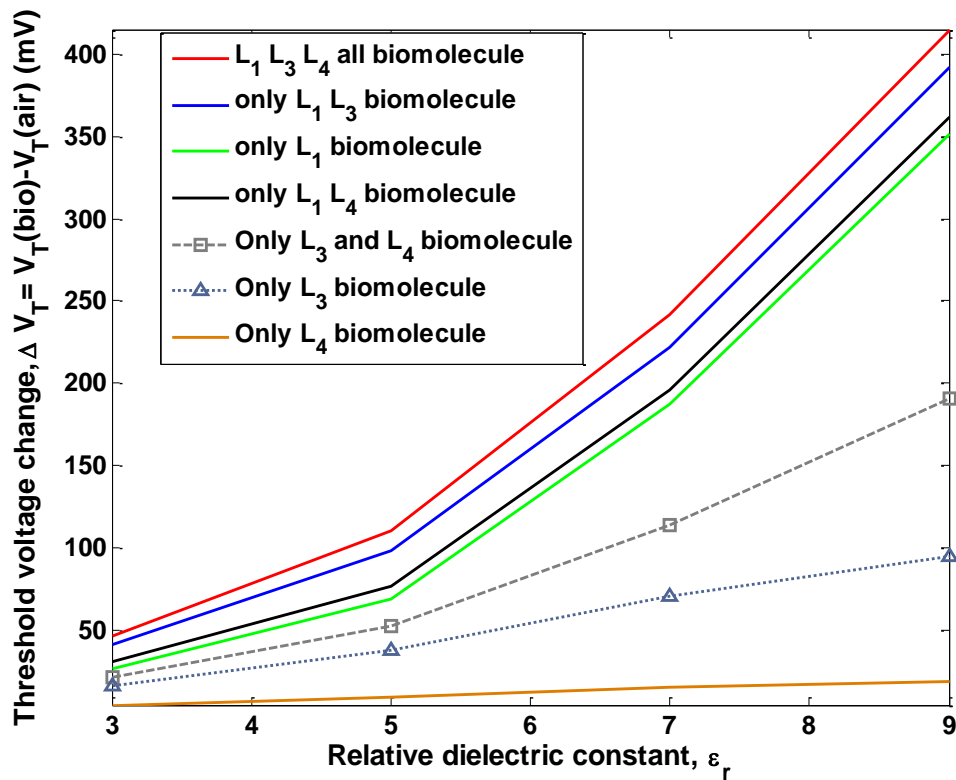


Figure 3.3 Variation of sensitivity factor ΔV_{th} for n-type DM-DG-MOSFETs for different positions of biomolecule in the cavity region when Region IV is connected to drain.

In this particular configuration, Region IV (as defined in Eq.3.4) is adjacent to the drain side and Region I (as defined in Eq.3.1) is connected to the source side. Any one of the region I, III and IV can be filled with biomolecules of different dielectric constants. The sensitivity (change in threshold voltage after the insertion of biomolecules with different dielectric constants) for different possible placements of biomolecule is shown in Figure 3.3. As shown in Figure 3.3 the best sensitivity is obtained when all of the three cavity regions are filled with biomolecules. This is logical in a sense that the higher the area coverage of biomolecule the better its influence is on device current. Hence, it will result in a greater change in threshold voltage of the device compared to the ‘no biomolecule’ case. Using the same reasoning it can be predicted that the next best sensitivity can be obtained when only Region III or Region IV is empty and all other cavity regions are filled with biomolecules. Results shown in Figure 3.3 actually support this prediction. However, a very interesting observation from Figure 3.3 is that for similar percentage of biomolecule coverage, the case in which biomolecules are more closely distributed to the center of the channel will yield better sensitivity. So, the case in which only L_4 (Region IV) is empty (of biomolecule) will result in a higher sensitivity than the case in which only L_3 (Region III) is empty. A reasonable explanation of such finding is, as the biomolecules get closer to the center of the channel, the gate voltage exerts a higher influence on channel potential barrier through capacitive coupling effect of biomolecule. Hence, such distribution of biomolecule will result in a higher change in drain current with variation of biomolecule’s dielectric constant. All other findings in Figure 3.3 can be explained by the similar reasoning described above. Therefore, in summary we can draw the following conclusions from the variation of biomolecule’s percentage and position in the cavity region.

- The greater the area coverage by biomolecule, higher the sensitivity of the DG FET in detecting biomolecule.
- The more closely located the biomolecules to the center of the channel; better the sensitivity of the biosensor.
- The higher the dielectric constant of the biomolecule, greater its effect on sensitivity.

3.5.3 Dependence of Sensitivity on Position of Biomolecule when Region I is connected to drain

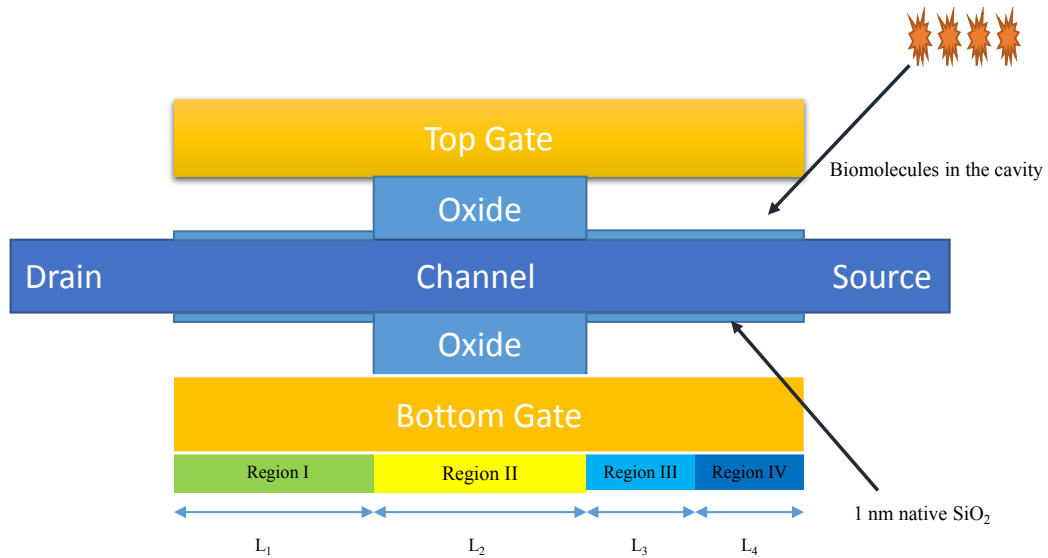


Figure 3.4 2D view (side) of Figure 3.1. Here Region I is connected to drain.

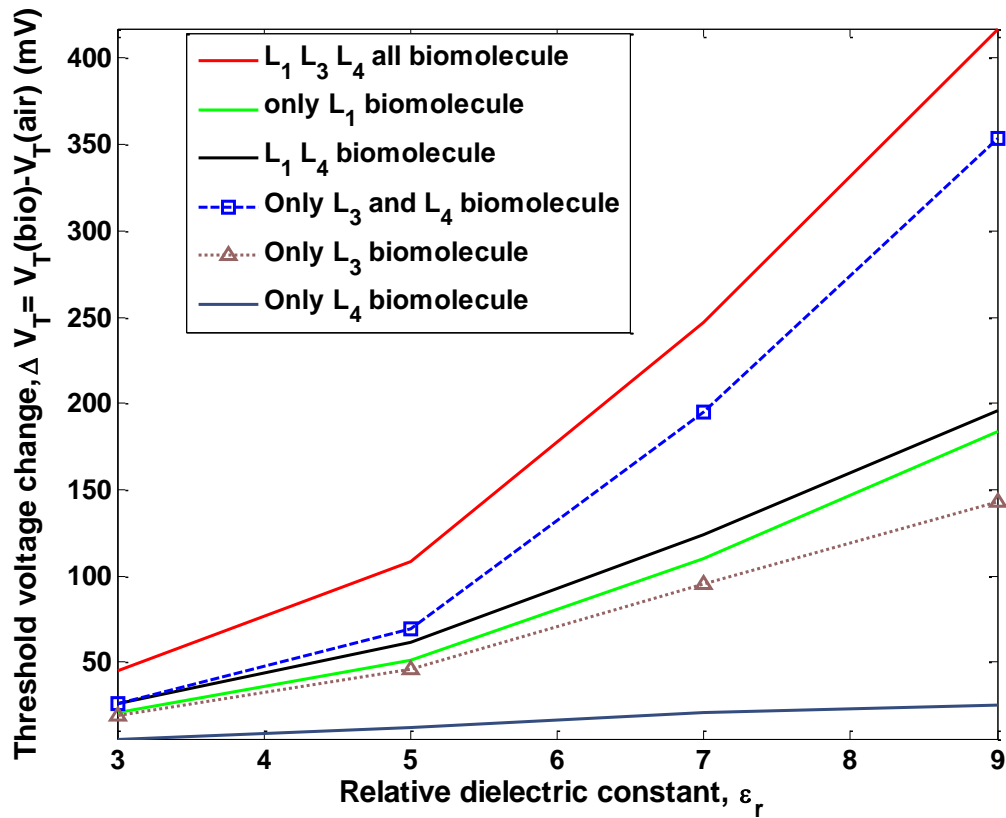


Figure 3.5 Variation of sensitivity factor ΔV_{th} for n-type DM-DG-MOSFETs for different positions of biomolecule in the cavity region when Region I is connected to drain.

In a slight different configuration, we can connect Region I (as defined in Eq.1) to the drain side and Region IV (as defined in Eq.4) can be attached to the source side. The dimensions of various regions are similar to that of the previous configuration. Our main purpose in this part is to investigate the effect of Drain to Source voltage on sensitivity of the device along with variation of biomolecule's position and percentage of area coverage. From Fig. 6, it can be observed that in symmetrical case, i.e. when all of the cavity regions are completely filled with biomolecule then interchanging the drain and source contact seems to have no effect on sensitivity. However, significant change in sensitivity can be found as we change the position and percentage of cavity region filled by biomolecules. For example, when only Region I and Region IV contain biomolecule, then sensitivity is markedly higher for the first configuration (where Region IV is connected to the drain) than the second case (where Region I is connected to the drain). Similarly the sensitivity is significantly higher for the first configuration (Region IV connected to drain) when only cavity in Region I contains biomolecule. However an opposite trend is observed for the cases where either one or both of Region III and IV are filled with biomolecule while Region I does not capture biomolecule. In these two cases actually the second configuration (Region I connected to drain) exhibits better sensitivity compared to the first one. In summary, it can be concluded from the above findings that for identical fill in factor of biomolecules in the cavity region, the larger the distance of the center of biomolecule from the drain end, higher the sensitivity of the device.

3.5.4 Summary

In this work, n-type JL-DM-DG-MOSFET have been proposed for the biosensing application. An analytical Drain current model is developed for both devices and results are verified with SILVACO ATLAS device Simulation tool. n-type JL-DM-DG-MOSFET shows good change in threshold voltage with the change of biomolecules. From the above results, it can be concluded that

- Higher the area coverage of biomolecule in the cavity region, greater the change in threshold voltage.
- Larger the distance of the center of biomolecule from the drain end, higher the sensitivity of the device.
- Higher the dielectric constant of the biomolecule, greater the change in threshold voltage hence better the sensitivity.

Chapter 4

Analytical Modeling of TMDC DMFET

4.1 Device Structure

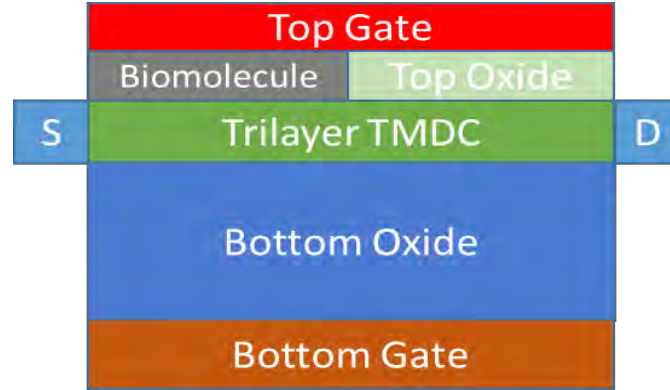


Figure 4.1 The MOSFET structure under consideration. It has a trilayer TMDC material channel sandwiched between top and bottom oxides and corresponding top and bottom gates. The channel, the source, and drain are highly n-doped regions of the same 2D material. Top oxide is etched one side to simulate effect of biomolecule on conductivity of the FET.

4.2 Differential System Establishment

To represent the physics and operation of the device a differential system must be devised first. However, we start with Figure 4.2 since the solution of that system can be extended to find out the solution of DMFET. Figure 4.2 shows the nominal n-type 2-D material MOSFET. Since the channel is very thin, it is reasonable to assume that electrostatic potential $\varphi(x, y)$ in the channel does not change in the direction along the top and bottom gate [29]. That is, it is safe to assume that in the channel potential $\varphi(x, y) \approx \varphi(x)$.

To get the differential system we need to apply the gauss's law in the infinitely small closed box shown in Figure 4.2. The box has height t_{ch} (depth of the 2D channel, ~ 2 nm), width W and infinitely small length ∇x . From Gauss's Law the relationship between the charge density (Q) inside the enclosed box and the electric field outside the enclosed box (\vec{E}) can be founded as:

$$\oint_s \epsilon \vec{E} \cdot \vec{ds} = Q \quad (4.1)$$

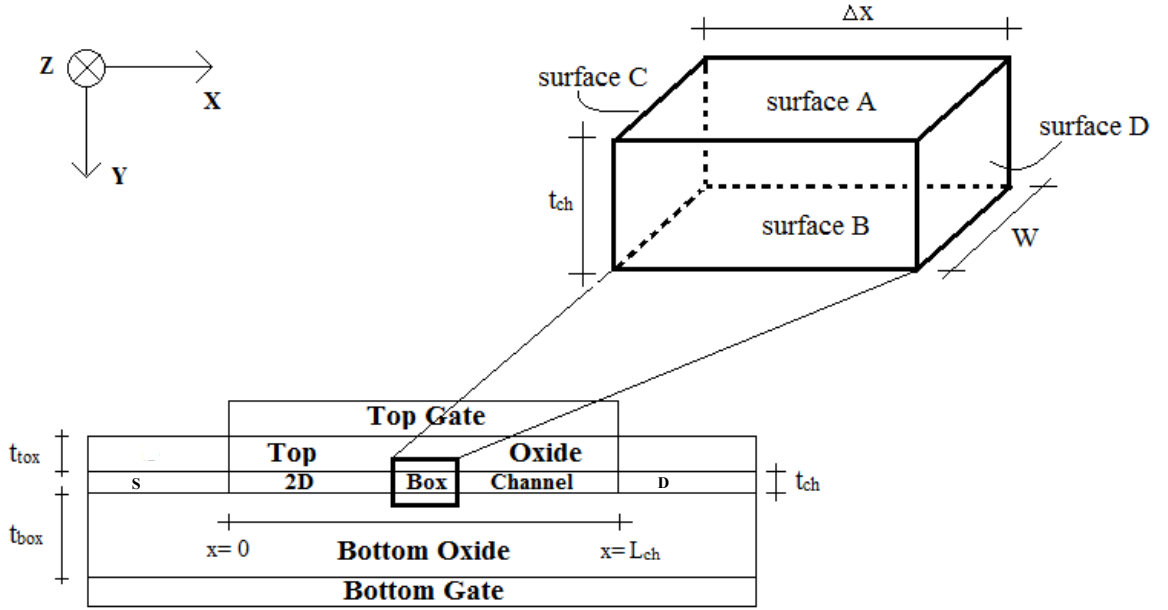


Figure 4.2 To establish the differential system for the 2D MOSFET an infinitesimal box is considered to which Gauss's Law ($\oint_s \epsilon \vec{E} \cdot \vec{ds} = Q$) is applied. The directions of the surface vectors are outward positive. Figure is taken from [85]

Here, ϵ is the dielectric permittivity of the material at each surface of the enclosed. Derivation starts by assuming the infinitely small box with width W , length Δx and depth of t_{ch} has a charge density of ΔQ . (See Figure 4.2)

After considering all the surface vectors from each side and then equating to the charge ΔQ , the result of algebraic manipulations will be in the following form with the application of gradual channel approximation. (The detailed derivation can be found elsewhere [85])

$$\frac{d^2 \varphi(x)}{dx^2} - K \varphi(x) = -A \quad (4.2)$$

Where,

$$A = \frac{kT}{q} K + G + \frac{q}{\epsilon_{ch} t_{ch}} N_D$$

$$K = \frac{\epsilon_{tox}}{t_{tox} \epsilon_{ch} t_{ch}} + \frac{\epsilon_{box}}{t_{box} \epsilon_{ch} t_{ch}}$$

$$G = \frac{\epsilon_{tox}}{t_{tox} \epsilon_{ch} t_{ch}} V'_{Gt} + \frac{\epsilon_{box}}{t_{tox} \epsilon_{ch} t_{ch}} V'_{Gb}$$

Table 4.1 Parameters used in this work for trilayer TMDC DMFET (Figure 4.1)

Parameter	Symbol	Value
Channel Thickness	t_{ch}	2 nm
Biomolecule Length (L_1)	L_{bio}	20 nm
Top Oxide Length (L_2)	L_{tox}	20 nm
Channel Length	$L_{ch} = L_{bio}(L_1) + L_{tox}(L_2)$	40 nm
Channel, Source and Drain Doping	N_D	$2.2 \times 10^{16} \text{ m}^{-2}$
Top Oxide Thickness (ZrO_2) (Biomolecule thickness)	t_{tox}/t_{bio}	9 nm
Bottom Oxide Thickness (SiO_2)	t_{box}	10 nm
Trilayer TMDC Electron Effective Mass	m^*	$0.52 \times 9.1 \times 10^{-31} \text{ kg}$
Trilayer TMDC Dielectric Permittivity	ϵ_{ch}	$5.2 \times 8.854 \times 10^{-12} \text{ Fm}^{-1}$
Metal-Semiconductor Work Function (top and bottom)	ϕ_{ms}	3.9 eV(Chosen considering bulk MoS_2)
ZrO_2 Dielectric Permittivity	ϵ_{tox}	$12.5 \times 8.854 \times 10^{-12} \text{ Fm}^{-1}$
SiO_2 Dielectric Permittivity	ϵ_{box}	$3.9 \times 8.854 \times 10^{-12} \text{ Fm}^{-1}$
Effective Gate Voltages	V'_{Gt}, V'_{bt}	$V'_{Gt} = V_{Gt} - \phi_{ms}$ $V'_{bt} = V_{bt} - \phi_{ms}$
Biomolecule dielectric constant	ϵ_{bio}	$(3 \text{ to } 9) \times 8.854 \times 10^{-12} \text{ Fm}^{-1}$

Equation 4.2 is a linear differential Equation with constant co-efficient. A closed form solution of this differential Equation is possible.

The complete solution of the Equation 4.2 is,

$$\varphi(x) = C_1 e^{\sqrt{K}x} + C_2 e^{-\sqrt{K}x} + \frac{A}{K} \quad (4.3)$$

For our device structure in Figure 4.1, we divide the whole channel into two regions, one under the biomolecule and one under ZrO_2 . For each region, we get two differential equations:

Region I: Under biomolecule (For $0 < L < L_{bio}$)

$$\frac{d^2\phi_1(x)}{dx^2} - K_1\phi_1(x) = -A_1 \quad (4.4)$$

Region II: Under top oxide ZrO_2 (For $L_{bio} < L < L_{ch}$)

$$\frac{d^2\phi_2(x)}{dx^2} - K_2\phi_2(x) = -A_2 \quad (4.5)$$

Solution of equations 4.4 and 4.5 will be in the form 4.3

$$\phi_1(x) = C_1 e^{\sqrt{K_1}x} + C_2 e^{-\sqrt{K_1}x} + \frac{A_1}{K_1} \quad (4.6)$$

Where,

$$A_1 = \frac{kT}{q} K_1 + G_1 + \frac{q}{\epsilon_{ch} t_{ch}} N_D$$

$$K_1 = \frac{\epsilon_{bio}}{t_{bio} \epsilon_{ch} t_{ch}} + \frac{\epsilon_{box}}{t_{box} \epsilon_{ch} t_{ch}}$$

$$G_1 = \frac{\epsilon_{bio}}{t_{bio} \epsilon_{ch} t_{ch}} V'_{Gt} + \frac{\epsilon_{box}}{t_{tox} \epsilon_{ch} t_{ch}} V'_{Gb}$$

$$\phi_2(x) = C_3 e^{\sqrt{K_2}(x-L_1)} + C_4 e^{-\sqrt{K_2}(x-L_1)} + \frac{A_2}{K_2} \quad (4.7)$$

Where,

$$A_2 = \frac{kT}{q} K_2 + G_2 + \frac{q}{\epsilon_{ch} t_{ch}} N_D$$

$$K_2 = \frac{\epsilon_{tox}}{t_{tox} \epsilon_{ch} t_{ch}} + \frac{\epsilon_{box}}{t_{box} \epsilon_{ch} t_{ch}}$$

$$G_2 = \frac{\epsilon_{tox}}{t_{tox} \epsilon_{ch} t_{ch}} V'_{Gt} + \frac{\epsilon_{box}}{t_{tox} \epsilon_{ch} t_{ch}} V'_{Gb}$$

4.3 Evaluating the Constants C_1 , C_2 , C_3 and C_4

For finding out four constants, we need four equations

$$\phi_1(x=0) = 0 \quad (4.8)$$

$$\phi_1(x=L_{bio}) = \phi_2(x=L_{bio}) \quad (4.9)$$

$$\frac{d\phi_1}{dx} = \frac{d\phi_2}{dx} \quad (\text{at } x=L_{bio}=L_1) \quad (4.10)$$

$$\phi_2(x=L_2+L_1) = V_{ds} \quad (4.11)$$

Solving (4.8) - (4.11), we get following four constant values.

$$C_1 = \frac{(A_{11} * D_1 + A_{12} * D_2 + A_{14} * D_4)}{Den}$$

$$C_2 = \frac{(A_{21} * D_1 + A_{22} * D_2 + A_{24} * D_4)}{Den}$$

$$C_3 = \frac{(A_{31} * D_1 + A_{32} * D_2 + A_{34} * D_4)}{Den}$$

$$C_4 = \frac{(A_{41} * D_1 + A_{42} * D_2 + A_{44} * D_4)}{Den}$$

The constant terms associated with C_1 to C_4 are given in the Appendix B.

4.4 Result and Discussion

When biomolecule enters the cavity, the potential profile changes according to the dielectric constant of the biomolecule.

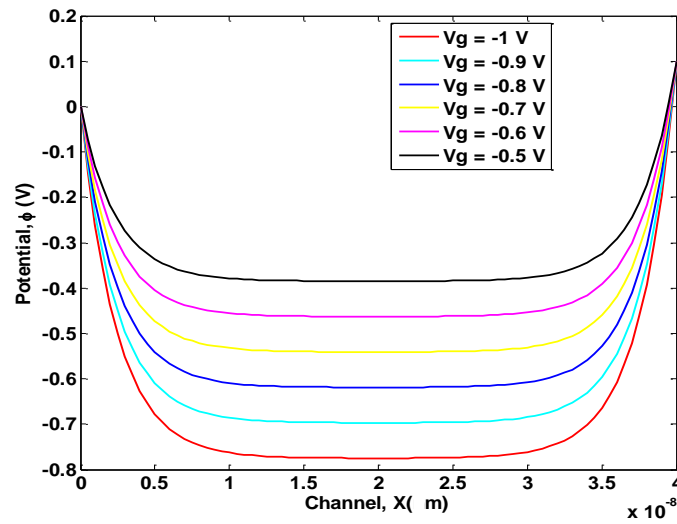


Figure 4.3 Potential profile when biomolecule dielectric constant is equal to top oxide dielectric constant.

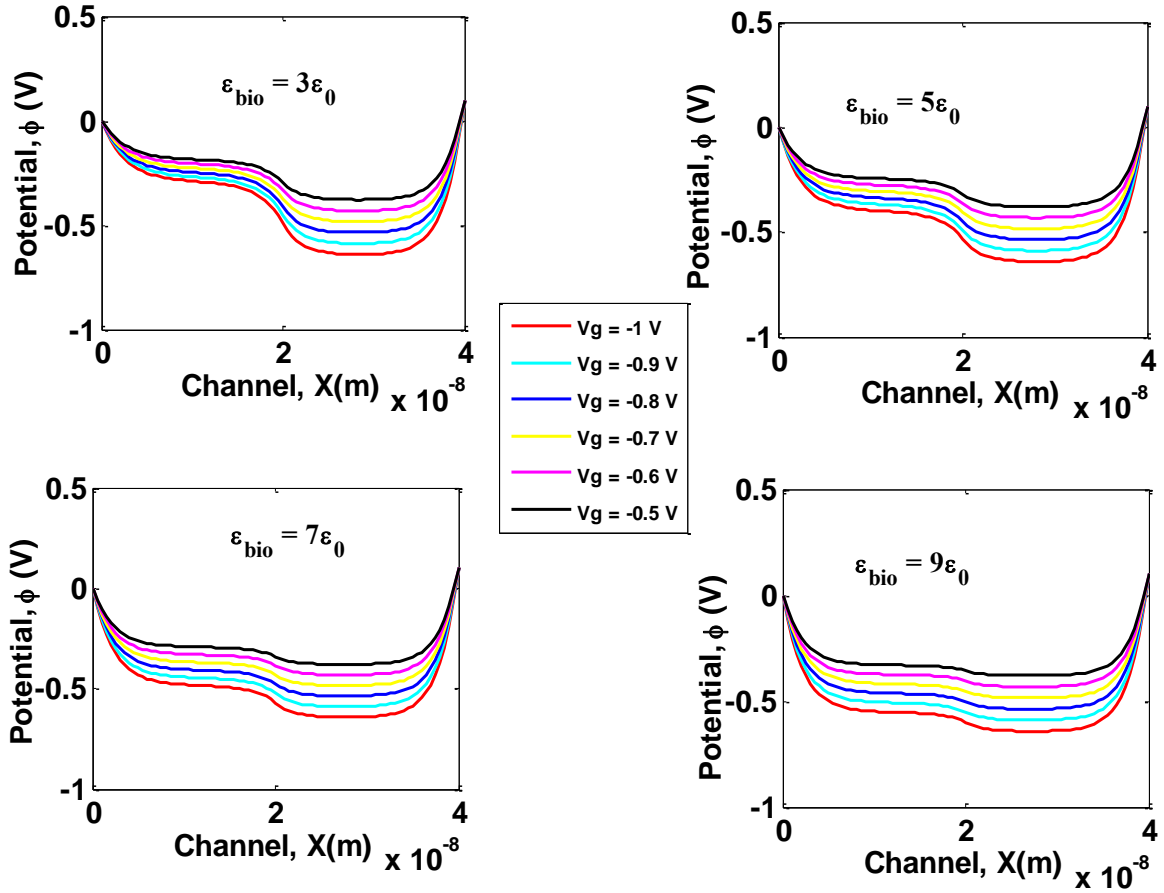


Figure 4.4 Potential profile when biomolecule's relative dielectric permittivity is equal to 3, 5, 7 and 9.

Drift diffusion equations are as follows[29], where n_{2D} , ϕ and V are carrier density, potential and quasi Fermi potential respectively.

$$n_{2D} = N_{DOS} e^{q(\phi - V)/kT}$$

$$N_{DOS} = \frac{2\pi mkT}{h^2}$$

$$I_{ds} = qWn_{2D}(x)\mu(x) \frac{dV(x)}{dx}$$

Though we have captured the effect of biomolecule on ϕ , its effect on V is still unexplored and subjected to future research. However, to predict the sensitivity of trilayer TMDC FET, we have used the NEGF current simulator described in the next section. For measuring sensitivity, we have used the following formulae (same as that of biosensor in chapter 2).

$$S = \frac{\Delta I_d}{I_d} = \frac{|I_d(bio) - I_d(air)|}{\min(I_d(bio), I_d(air))}$$

4.5 DMFET Simulation using NEGF approach

4.5.1 Simulation approach:

For the materials (MX₂) and dimensions of interest, it becomes essential to evaluate the electrical characteristics of MX₂ heterostructure based FETs using quantum transport. An elegant approach to solve ballistic transport in these emerging material devices consists of the self-consistent solution of Poisson and Schrodinger equation in an NEGF framework with tight binding (TB) Hamiltonian. In this part, we use two-band TB Hamiltonian for trilayer MX₂ materials, with an open source quantum transport simulation framework[86]. For trilayer MX₂ heterostructure materials, the two-band Hamiltonian parameters are calculated using the effective mass of conduction (n-FET) or valence band (p-FET), and the bandgap of the material[87].

The electron and hole concentrations are calculated by means of solving the Schrödinger equation using the NEGF formalism that employs the open boundary conditions.

The Green's function can be expressed as

$$G^m(E) = (EI - H - \Sigma_S^m(E) - \Sigma_D^m(E))^{-1} \quad (4.12)$$

Where E represents the energy, I stands for the identity matrix, H is the Hamiltonian of the TMD, and Σ_S^m and Σ_D^m represent the self- energies of the source and drain, respectively. While carrying out the simulations, the transport is assumed ballistic completely. The spectral density matrices at source and drain contacts can be calculated as-

$$A_S^m(E) = G^m(E)\Gamma_S^m(E)G^{m\dagger}(E) \quad \text{and} \quad A_D^m(E) = G^m(E)\Gamma_D^m(E)G^{m\dagger}(E) \quad (4.13)$$

Where, $\Gamma_S^m(E)$ and $\Gamma_D^m(E)$ are the spectral broadening matrices at source and drain contacts given by-

$$\Gamma_S^m(E) = i \left(\Sigma_S^m(E) - \Sigma_S^{m\dagger}(E) \right) \quad \text{and} \quad \Gamma_D^m(E) = i \left(\Sigma_D^m(E) - \Sigma_D^{m\dagger}(E) \right) \quad (4.14)$$

The 2D electron density can now be calculated as-

$$n_x^m = \frac{1}{2\pi a} 2 \left(\frac{2m_z^* k_B T}{\pi \hbar^2} \right)^{1/2} \int_{-\infty}^{\infty} [\mathfrak{F}_{-1/2} \left(\frac{\mu_S - E}{k_B T} \right) \text{diag}(A_S^m(E)) + \mathfrak{F}_{-1/2} \left(\frac{\mu_D - E}{k_B T} \right) \text{diag}(A_D^m(E))] dE \quad (4.15)$$

Where, m_z^* is the transverse effective mass (along z-axis), μ_S and μ_D are source and drain Fermi levels respectively and a is grid size. Function $\mathfrak{F}_{-1/2}$ denotes Fermi-Dirac integral of order $-1/2$. 3D electron density is obtained by multiplying n_x^m with the transverse wave

function $|\overline{\psi^m}(y)|^2$. This transverse wave function has been calculated from solving Schrodinger equations at discrete points along the channel.

$$n_{3D}^m(x, y) = n_x^m |\overline{\psi^m}(y)|^2 \quad (4.16)$$

The total electron density is obtained by summing the above equation for all subbands. The ballistic current is calculated as-

$$I = \frac{q}{2\pi\hbar} 2 \left(\frac{2m_z^* k_B T}{\pi\hbar^2} \right)^{1/2} \int_{-\infty}^{\infty} [\mathfrak{F}_{-1/2} \left(\frac{\mu_S - E}{k_B T} \right) - \mathfrak{F}_{-1/2} \left(\frac{\mu_D - E}{k_B T} \right)] T(E) dE \quad (4.17)$$

Where, $T(E)$ is obtained by summing the transmission coefficient $T^m(E)$ over all subbands. $T^m(E)$ is given by-

$$T^m(E) = \text{trace}(\Gamma_S^m(E) G^m(E) \Gamma_D^m(E) G^{m\dagger}(E)) \quad (4.18)$$

It needs to be pointed out that the current model used only considers one-dimensional transport between the source and drain reservoirs and that the leakage gate current is not considered. The Green's function is determined using the recursive Green's function technique. Emphasis is needed on the definition of each self-energy matrix, which can be construed as one of the boundary conditions of the Schrödinger equation. Complete ViDES code is presented in Appendix C.

4.6 Result and Discussion

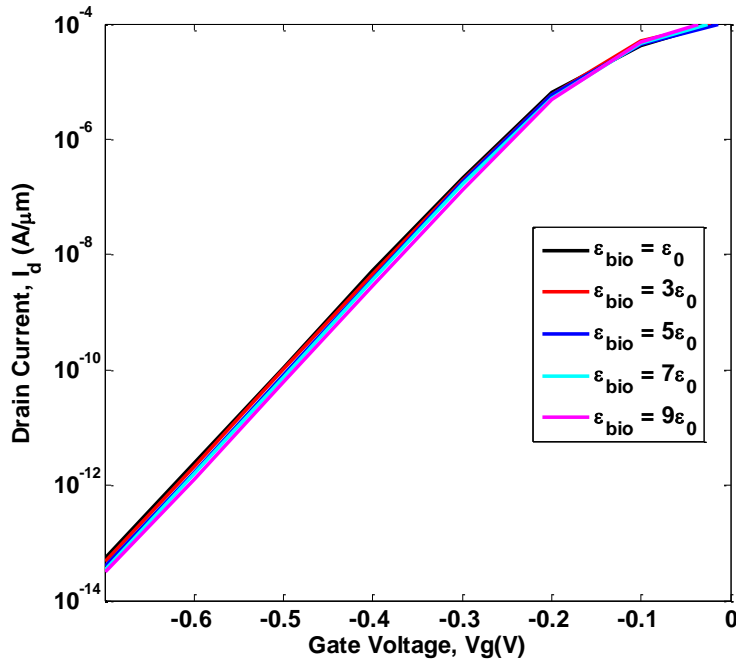


Figure 4.5 $I_d - V_G$ characteristics of dielectrically modulated trilayer TMDC FET.

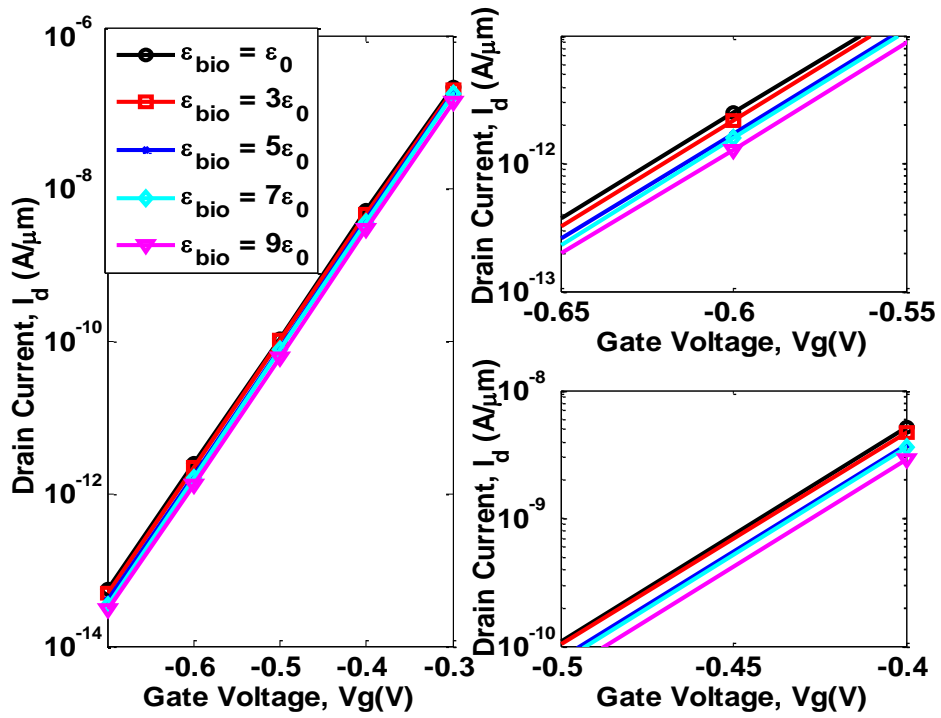


Figure 4.6 $I_d - V_G$ characteristics of dielectrically modulated trilayer TMDC FET. (Zoomed in subthreshold region)

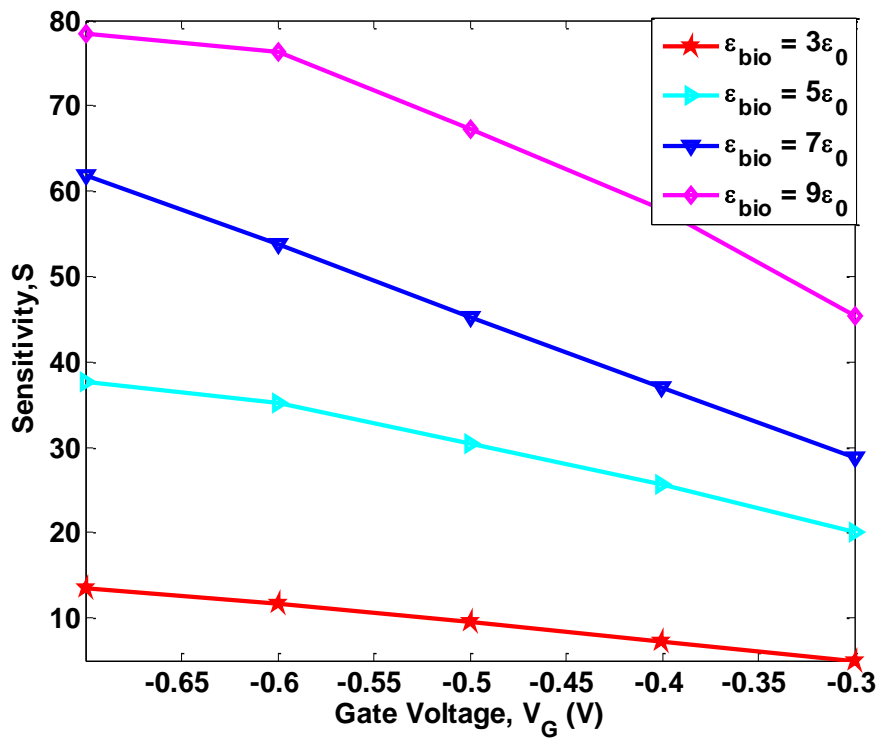


Figure 4.7 Sensitivity in the subthreshold region

Chapter 5

Conclusion

5.1 Summary

The electrostatic correlation of charged biomolecules (such as DNA) or ions to the nanoscale semiconductor devices and its corresponding electronic responses are studied. We developed a numerical model to explain the sensitivity of biomolecule detection and its dependence on various physical and operating parameters in double-gated FET devices. In contrast to the conventional studies on DGFETs focusing on their superior electrostatics to the planar transistors, our results demonstrate that it is possible to amplify the detection signal, in the presence of electrolyte screening, via the proper combination of the sensor geometry, bias conditions, insulating materials, buffer conditions, and operation mode in two independent gates. In this work, we have also investigated bio-sensing application in dry environment. An analytical Drain current model was developed for devices and surface potential has been verified with “SILVACO ATLAS” device simulation tool. Good change in threshold voltage, ΔV_{th} was observed with the change of biomolecules. We varied the position and percentage of area in nanogap cavity covered by biomolecule to find out their effects on sensitivity. From such variation, it was found that maximum sensitivity is obtained when all of the cavity regions are filled with biomolecule. Moreover, for cavity regions with partially filled biomolecule, the sensitivity can be enhanced by moving the biomolecules more towards the center of the channel along carrier transport direction from the drain side.

5.2 Suggestions for Future Work

- 1) Monolayer TMDC material can be used as channel material and relative comparison on performance of such pH and biosensor can be investigated.
- 2) Detection of other biomolecules like biotin-streptavidin pair, Avidin, and mRNA can be studied.
- 3) More complex electrolyte buffer containing divalent salt ions can be introduced and their effect on Debye screening can be studied.
- 4) More accurate and computationally expensive current model can be used to predict device current more realistically.

- 5) Effect of buffer ion concentration on sensitivity can be investigated.
- 6) For dielectrically modulated FET biosensor, different oxide material other than SiO₂ can be introduced and their effects on sensitivity can be investigated.
- 7) Prospect of other device structure like Tunnel FETs as biosensors can be investigated.

References

- [1] C. J. L. Murray and C. Stein, "Project : Aims , Methods and Data Sources .," 2001.
- [2] M. F. Reed, M. Molloy, E. L. Dalton, and J. A. Howington, "Survival after resection for lung cancer is the outcome that matters," *Am. J. Surg.*, vol. 188, no. 5, pp. 598–602, 2004.
- [3] A. M. Ward, J. W. F. Catto, and F. C. Hamdy, "Prostate speci ® c antigen : biology , biochemistry and available," *Ann Clin Biochem*, vol. 1, no. 38, pp. 633–651, 2001.
- [4] A. Noy, A. B. Artyukhin, and N. Misra, "Bionanoelectronics with 1D materials," *Materials Today*, vol. 12, no. 9. Elsevier Ltd, pp. 22–31, 2009.
- [5] J. O. Lee, H. M. So, E. K. Jeon, H. Chang, K. Won, and Y. H. Kim, "Aptamers as molecular recognition elements for electrical nanobiosensors," *Anal. Bioanal. Chem.*, vol. 390, no. 4, pp. 1023–1032, 2008.
- [6] E. B. Cooper, S. Gaudet, P. K. Sorger, and S. R. Manalis, "Electronic detection of DNA by its intrinsic molecular charge," in *Proceedings of the National Academy of Sciences*, 2002, vol. 99, no. 22, pp. 14142–14146.
- [7] P. Bergveld, "Thirty years of ISFETOLOGY What happened in the past 30 years and what may happen in the next 30 years," *Sensors and Actuators*, vol. 88, pp. 1–20, 2003.
- [8] P. Ir, P. B. Em, and F. Ee, "ISFET , Theory and Practice," in *IEEE Sensor Conference in Toronto*, 2003, no. October, pp. 1–26.
- [9] G. Zheng, F. Patolsky, Y. Cui, W. U. Wang, and C. M. Lieber, "Multiplexed electrical detection of cancer markers with nanowire sensor arrays," *Nat. Biotechnol.*, vol. 23, no. 10, pp. 1294–1301, 2005.
- [10] A. Star, J. C. P. Gabriel, K. Bradley, and G. Grüner, "Electronic detection of specific protein binding using nanotube FET devices," *Nano Lett.*, vol. 3, no. 4, pp. 459–463, 2003.
- [11] J. F. Klemic, E. Stern, and M. A. Reed, "Hotwiring biosensors Nanowire sensors decorated with specific capture molecules can detect minute quantities of biological and chemical species .," *Nat. Biotechnol.*, vol. 19, no. 10, pp. 924–925, 2001.
- [12] P. R. Nair and M. A. Alam, "Screening-Limited Response of NanoBiosensors," *Nano Lett.*, vol. 8, no. 5, pp. 1281–1285, 2008.
- [13] Y. Liu, K. Lilja, C. Heitzinger, and R. W. Dutton, "Overcoming the screening-induced performance limits of nanowire biosensors: A simulation study on the effect of electro-diffusion flow," *Tech. Dig. - Int. Electron Devices Meet. IEDM*, pp. 10–13, 2008.
- [14] R. S. Gaster, D. A. Hall, C. H. Nielsen, S. J. Osterfeld, H. Yu, K. E. Mach, R. J. Wilson, B. Murmann, J. C. Liao, S. S. Gambhir, and S. X. Wang, "Matrix-insensitive protein assays push the limits of biosensors in medicine.," *Nat. Med.*, vol. 15, no. 11, pp. 1327–32, 2009.
- [15] H. Lee, E. Sun, D. Ham, and R. Weissleder, "Chip-NMR biosensor for detection and molecular analysis of cells.," *Nat. Med.*, vol. 14, no. 8, pp. 869–874, 2008.

- [16] "ITRS Roadmap 2013." [Online]. Available: <http://www.itrs2.net/2013-itrs.html>.
- [17] S. Z. Butler, S. M. Hollen, L. Cao, Y. Cui, J. A. Gupta, H. R. Gutierrez, T. F. Heinz, S. S. Hong, J. Huang, A. F. Ismach, E. Johnston-Halperin, M. Kuno, V. V. Plashnitsa, R. D. Robinson, R. S. Ruoff, S. Salahuddin, J. Shan, L. Shi, M. G. Spencer, M. Terrones, W. Windl, and J. E. Goldberger, "Progress, challenges, and opportunities in two-dimensional materials beyond graphene," *ACS Nano*, vol. 7, no. 4, pp. 2898–2926, 2013.
- [18] C. N. R. Rao, K. Gopalakrishnan, and U. Maitra, "Comparative Study of Potential Applications of Graphene, MoS₂, and Other Two-Dimensional Materials in Energy Devices, Sensors, and Related Areas.," *ACS Appl. Mater. Interfaces*, vol. 7, no. 15, pp. 7809–32, 2015.
- [19] H. Peelaers and C. G. Van de Walle, "Effects of strain on band structure and effective masses in MoS₂," *Phys. Rev. B*, vol. 86, no. 24, p. 241401, 2012.
- [20] E. S. Kadantsev and P. Hawrylak, "Electronic structure of a single MoS₂ monolayer," *Solid State Commun.*, vol. 152, no. 10, pp. 909–913, 2012.
- [21] H. Terrones, F. López-Urías, and M. Terrones, "Novel hetero-layered materials with tunable direct band gaps by sandwiching different metal disulfides and diselenides.," *Sci. Rep.*, vol. 3, p. 1549, 2013.
- [22] N. Lu, H. Guo, L. Li, J. Dai, L. Wang, W.-N. Mei, X. Wu, and X. C. Zeng, "MoS₂/MX₂ heterobilayers: bandgap engineering via tensile strain or external electrical field.," *Nanoscale*, vol. 6, no. 5, pp. 2879–86, 2014.
- [23] J. He, K. Hummer, and C. Franchini, "Stacking effects on the electronic and optical properties of bilayer transition metal dichalcogenides MoS₂, MoSe₂, WS₂, and WSe₂," *Phys. Rev. B*, vol. 89, no. 7, p. 075409, 2014.
- [24] B. Radisavljevic, A. Radenovic, J. Brivio, V. Giacometti, and A. Kis, "Single-layer MoS₂ transistors," *Nat. Nanotechnol.*, vol. 6, no. 3, pp. 147–50, 2011.
- [25] Y. Yoon, K. Ganapathi, and S. Salahuddin, "How good can monolayer MoS₂ transistors be?," *Nano Lett.*, vol. 11, no. 9, pp. 3768–3773, 2011.
- [26] S. Das, H. Y. Chen, A. V. Penumatcha, and J. Appenzeller, "High performance multilayer MoS₂ transistors with scandium contacts," *Nano Lett.*, vol. 13, no. 1, pp. 100–105, 2013.
- [27] W. Liu, J. Kang, D. Sarkar, Y. Khatami, D. Jena, and K. Banerjee, "Role of metal contacts in designing high-performance monolayer n-type WSe₂ field effect transistors," *Nano Lett.*, vol. 13, no. 5, pp. 1983–1990, 2013.
- [28] H. Fang, S. Chuang, T. C. Chang, K. Takei, T. Takahashi, and A. Javey, "High-performance single layered WSe₂ p-FETs with chemically doped contacts," *Nano Lett.*, vol. 12, no. 7, pp. 3788–3792, 2012.
- [29] W. Cao, J. Kang, W. Liu, and K. Banerjee, "A compact current-voltage model for 2D semiconductor based field-effect transistors considering interface traps, mobility degradation, and inefficient doping effect," *IEEE Trans. Electron Devices*, vol. 61, no. 12, pp. 4282–4290, 2014.
- [30] W. Cao, J. Kang, D. Sarkar, W. Liu, and K. Banerjee, "2D Semiconductor FETs - Projections and Design for Sub-10 nm VLSI," *IEEE Trans. Electron Devices*, vol. 62,

- no. 11, pp. 3459–3469, 2015.
- [31] S. V. Suryavanshi and E. Pop, “Physics-Based Compact Model for Circuit Simulations of 2-Dimensional Semiconductor Devices,” vol. 569, no. 1992, pp. 9–10, 2015.
- [32] G. S. Duesberg, “Heterojunctions in 2D semiconductors: A perfect match,” *Nat. Mater.*, vol. 13, no. 12, pp. 1075–1076, 2014.
- [33] C. Huang, S. Wu, A. M. Sanchez, J. J. P. Peters, R. Beanland, J. S. Ross, P. Rivera, W. Yao, D. H. Cobden, and X. Xu, “Lateral heterojunctions within monolayer MoSe₂–WSe₂ semiconductors,” *Nat. Mater.*, vol. 13, no. 12, pp. 1–6, 2014.
- [34] M. O. Li, D. Esseni, J. J. Nahas, D. Jena, and H. G. Xing, “Two-dimensional heterojunction interlayer tunneling field effect transistors (Thin-TFETs),” *IEEE J. Electron Devices Soc.*, vol. 3, no. 3, pp. 200–207, 2015.
- [35] N. Lu, H. Guo, L. Wang, X. Wu, and X. C. Zeng, “van der Waals trilayers and superlattices: modification of electronic structures of MoS₂ by intercalation,” *Nanoscale*, pp. 4566–4571, 2014.
- [36] A. K. Geim and K. S. Novoselov, “The rise of graphene,” *Nat. Mater.*, pp. 183–191, 2007.
- [37] Y. Liu, X. Dong, and P. Chen, “Biological and chemical sensors based on graphene materials,” *Chem. Soc. Rev.*, vol. 41, no. 6, p. 2283, 2012.
- [38] H. Li, Z. Yin, Q. He, H. Li, X. Huang, G. Lu, D. W. H. Fam, A. I. Y. Tok, Q. Zhang, and H. Zhang, “Fabrication of single- and multilayer MoS₂ film-based field-effect transistors for sensing NO at room temperature,” *Small*, vol. 8, no. 1, pp. 63–67, 2012.
- [39] F. K. Perkins, a L. Friedman, E. Cobas, P. M. Campbell, G. G. Jernigan, and B. T. Jonker, “Chemical vapor sensing with monolayer MoS₂,” *Nano Lett.*, vol. 13, no. 2, pp. 668–673, 2013.
- [40] L. Wang, Y. Wang, J. I. Wong, T. Palacios, J. Kong, and H. Y. Yang, “Functionalized MoS₂ nanosheet-based field-effect biosensor for label-free sensitive detection of cancer marker proteins in solution,” *Small*, vol. 10, no. 6, pp. 1101–1105, 2014.
- [41] D. Sarkar, W. Liu, X. Xie, A. C. Anselmo, S. Mitragotri, and K. Banerjee, “MoS₂ Field-Effect Transistor for Next-Generation Biosensors,” *ACS Nano*, vol. 8, no. 4, pp. 3992–4003, 2014.
- [42] W. Wu, D. De, S. C. Chang, Y. Wang, H. Peng, J. Bao, and S. S. Pei, “High mobility and high on/off ratio field-effect transistors based on chemical vapor deposited single-crystal MoS₂ grains,” *Appl. Phys. Lett.*, vol. 102, no. 14, pp. 1–5, 2013.
- [43] H. Nam, B. R. Oh, P. Chen, J. S. Yoon, S. Wi, M. Chen, K. Kurabayashi, and X. Liang, “Two different device physics principles for operating MoS₂ transistor biosensors with femtomolar-level detection limits,” *Appl. Phys. Lett.*, vol. 107, no. 1, pp. 1–7, 2015.
- [44] J. Lee, P. Dak, Y. Lee, H. Park, W. Choi, M. a Alam, and S. Kim, “Two-dimensional layered MoS₂ biosensors enable highly sensitive detection of biomolecules,” *Sci. Rep.*, vol. 4, p. 7352, 2014.
- [45] H. Nam, B.-R. Oh, P. Chen, M. Chen, S. Wi, W. Wan, K. Kurabayashi, and X. Liang, “Multiple MoS₂ Transistors for Sensing Molecule Interaction Kinetics,” *Sci. Rep.*, vol.

- 5, no. MAY, p. 10546, 2015.
- [46] P. Bergveld, "Development, operation, and application of the ion-sensitive field-effect transistor as a tool for electrophysiology.," *IEEE Trans. Biomed. Eng.*, vol. 19, no. 5, pp. 342–351, 1972.
- [47] H. Im, X.-J. Huang, B. Gu, and Y.-K. Choi, "A dielectric-modulated field-effect transistor for biosensing.," *Nat. Nanotechnol.*, vol. 2, no. 7, pp. 430–4, 2007.
- [48] C. Kim, C. Jung, H. G. Park, and Y. Choi, "Novel Dielectric-Modulated Field-Effect Transistor for Label-Free DNA Detection," *BIOCHIP*, vol. 2, no. 2, pp. 127–134, 2008.
- [49] P. Giannozzi, S. Baroni, N. Bonini, M. Calandra, R. Car, C. Cavazzoni, D. Ceresoli, G. L. Chiarotti, M. Cococcioni, I. Dabo, A. Dal Corso, S. de Gironcoli, S. Fabris, G. Fratesi, R. Gebauer, U. Gerstmann, C. Gougoussis, A. Kokalj, M. Lazzeri, L. Martin-Samos, N. Marzari, F. Mauri, R. Mazzarello, S. Paolini, A. Pasquarello, L. Paulatto, C. Sbraccia, S. Scandolo, G. Sclauzero, A. P. Seitsonen, A. Smogunov, P. Umari, and R. M. Wentzcovitch, "QUANTUM ESPRESSO: a modular and open-source software project for quantum simulations of materials.," *J. Phys. Condens. Matter*, vol. 21, no. 39, p. 395502, 2009.
- [50] C. Hartwigsen, S. Goedecker, and J. Hutter, "Relativistic separable dual-space Gaussian pseudopotentials from H to Rn," *Phys. Rev. B*, vol. 58, no. 7, pp. 3641–3662, 1998.
- [51] K. Datta and Q. D. M. Khosru, "Electronic Properties of MoS₂/MX₂/MoS₂ Trilayer Heterostructures: A First Principle Study," *ECS J. Solid State Sci. Technol.*, vol. 5, no. 11, pp. Q3001–Q3007, 2016.
- [52] H. Monkhorst and J. Pack, "Special points for Brillouin zone integrations," *Phys. Rev. B*, vol. 13, no. 12, pp. 5188–5192, 1976.
- [53] S. Birner, C. Uhl, M. Bayer, and P. Vogl, "Theoretical model for the detection of charged proteins with a silicon-on-insulator sensor," *J. Phys. Conf. Ser.*, vol. 107, p. 012002, 2008.
- [54] J. Go, P. R. Nair, B. Reddy, B. Dorvel, R. Bashir, and M. A. Alam, "Beating the Nernst limit of 59mV/pH with double-gated nano-scale field-effect transistors and its applications to ultra-sensitive DNA biosensors," *Tech. Dig. - Int. Electron Devices Meet. IEDM*, vol. 2, pp. 202–205, 2010.
- [55] D. Landheer, G. Aers, W. R. McKinnon, M. J. Deen, and J. C. Ranuarez, "Model for the field effect from layers of biological macromolecules on the gates of metal-oxide-semiconductor transistors," *J. Appl. Phys.*, vol. 98, no. 4, 2005.
- [56] D. Jiménez, "Drift-diffusion model for single layer transition metal dichalcogenide field-effect transistors," *Appl. Phys. Lett.*, vol. 101, no. 24, 2012.
- [57] M. J. Spijkman, J. J. Brondijk, T. C. T. Geuns, E. C. P. Smits, T. Cramer, F. Zerbetto, P. Stolar, F. Biscarini, P. W. M. Blom, and D. M. De Leeuw, "Dual-gate organic field-effect transistors as potentiometric sensors in aqueous solution," *Adv. Funct. Mater.*, vol. 20, no. 6, pp. 898–905, 2010.
- [58] J. Go, P. R. Nair, and M. A. Alam, "Theory of signal and noise in double-gated nanoscale electronic pH sensors," *J. Appl. Phys.*, vol. 112, no. 3, 2012.
- [59] E. Performance, S.-I. F. Transistors, M. T. O. Layers, and E. Solution, "Electrical

- Performance of Silicon-on- Insulator Field-Effect Transistors with Multiple Top-Gate Organic Layers in,” *ACS Nano*, vol. 4, no. 8, pp. 4601–4608, 2010.
- [60] X. P. A. Gao, G. Zheng, and C. M. Lieber, “Subthreshold regime has the optimal sensitivity for nanowire FET biosensors,” *Nano Lett.*, vol. 10, no. 2, pp. 547–552, 2010.
- [61] M. Waleed Shinwari, M. Jamal Deen, and D. Landheer, “Study of the electrolyte-insulator-semiconductor field-effect transistor (EISFET) with applications in biosensor design,” *Microelectron. Reliab.*, vol. 47, no. 12, pp. 2025–2057, 2007.
- [62] M. C. Pirrung, “How to make a DNA chip,” *Angew. Chemie - Int. Ed.*, vol. 41, no. 8, pp. 1276–1289, 2002.
- [63] M. W. S. R. S. Cobbold, “Basic Properties of the Electrolyte-SiO₂-Si System ;,” *IEEE Trans. Electron Devices*, no. 1, pp. 1805–1815, 1979.
- [64] E. Stern, R. Wagner, F. J. Sigworth, R. Breaker, T. M. Fahmy, and M. A. Reed, “Importance of the debye screening length on nanowire field effect transistor sensors,” *Nano Lett.*, vol. 7, no. 11, pp. 3405–3409, 2007.
- [65] F. Puppo, M.-A. Doucey, T. S. Y. Moh, G. Pandraud, P. M. Sarro, G. De Micheli, and S. Carrara, “Femto-molar sensitive field effect transistor biosensors based on silicon nanowires and antibodies,” pp. 1–4, 2013.
- [66] Ajay, R. Narang, M. Gupta, and M. Saxena, “Investigation of Dielectric-Modulated Double-Gate Junctionless MOSFET for detection of biomolecules,” *2013 Annu. IEEE India Conf. INDICON 2013*, vol. 2, pp. 1–6, 2013.
- [67] C. W. Lee, A. Afzalian, N. D. Akhavan, R. Yan, I. Ferain, and J. P. Colinge, “Junctionless multigate field-effect transistor,” *Appl. Phys. Lett.*, vol. 94, no. 5, pp. 13–15, 2009.
- [68] J.-P. Colinge, C.-W. Lee, A. Afzalian, N. D. Akhavan, R. Yan, I. Ferain, P. Razavi, B. O’Neill, A. Blake, M. White, A.-M. Kelleher, B. McCarthy, and R. Murphy, “Nanowire transistors without junctions,” *Nat. Nanotechnol.*, vol. 5, no. 3, pp. 225–229, 2010.
- [69] C. W. Lee, A. Borne, I. Ferain, A. Afzalian, R. Yan, N. Dehdashti Akhavan, P. Razavi, and J. P. Colinge, “High-temperature performance of silicon junctionless MOSFETs,” *IEEE Trans. Electron Devices*, vol. 57, no. 3, pp. 620–625, 2010.
- [70] F. Jazaeri, L. Barbut, A. Koukab, and J. M. Sallese, “Analytical model for ultra-thin body junctionless symmetric double gate MOSFETs in subthreshold regime,” *Solid. State. Electron.*, vol. 82, pp. 103–110, 2013.
- [71] S. Kim, J. H. Ahn, T. J. Park, S. Y. Lee, and Y. K. Choi, “A biomolecular detection method based on charge pumping in a nanogap embedded field-effect-transistor biosensor,” *Appl. Phys. Lett.*, vol. 94, no. 24, pp. 1–4, 2009.
- [72] K.-W. Lee, S.-J. Choi, J.-H. Ahn, D.-I. Moon, T. J. Park, S. Y. Lee, and Y.-K. Choi, “An underlap field-effect transistor for electrical detection of influenza,” *Appl. Phys. Lett.*, vol. 96, no. 3, p. 33703, 2010.
- [73] R. Narang, M. Saxena, and M. Gupta, “Comparative Analysis of Dielectric-Modulated FET and TFET-Based Biosensor,” *IEEE Trans. Nanotechnol.*, vol. 14, no. 3, pp. 427–435, 2015.

- [74] Ajay, R. Narang, M. Saxena, and M. Gupta, "Analysis of gate underlap channel double gate MOS transistor for electrical detection of bio-molecules," *Superlattices Microstruct.*, vol. 88, pp. 225–243, 2015.
- [75] Ajay, R. Narang, M. Saxena, and M. Gupta, "Drain Current Model of a Four-Gate Dielectric Modulated MOSFET for Application as a Biosensor," *IEEE Trans. Electron Devices*, vol. 62, no. 8, pp. 2636–2644, 2015.
- [76] Ajay, R. Narang, M. Saxena, and M. Gupta, "Investigation of dielectric modulated (DM) double gate (DG) junctionless MOSFETs for application as a biosensors," *Superlattices Microstruct.*, vol. 85, pp. 557–572, 2015.
- [77] R. Narang, S. S. Member, M. Saxena, and S. S. Member, "Dielectric Modulated Tunnel Field-Effect Transistor — A Biomolecule Sensor," vol. 33, no. 2, pp. 266–268, 2012.
- [78] C. Kim, J. Ahn, K. Lee, C. Jung, H. G. Park, and Y. Choi, "A New Sensing Metric to Reduce Data Fluctuations in a Nanogap-Embedded Field-Effect Transistor Biosensor," vol. 59, no. 10, pp. 2825–2831, 2012.
- [79] "TCAD Sentaurus Device User Manual," 2013.
- [80] S. Busse, V. Scheumann, B. Menges, and S. Mittler, "Sensitivity studies for specific binding reactions using the biotin/streptavidin system by evanescent optical methods," *Biosens. Bioelectron.*, vol. 17, no. 8, pp. 704–710, 2002.
- [81] D.-X. Xu, A. Densmore, S. Janz, P. Waldron, T. Mischki, G. Lopinski, A. Del age, P. Cheben, J. Lapointe, B. Lamontagne, and J. H. Schmid, "Spiral-path high-sensitivity silicon photonic wire molecular sensor with temperature-independent response.," *Opt. Lett.*, vol. 33, no. 6, pp. 596–8, 2008.
- [82] E. Makarona, E. Kapetanakis, D. M. Velessiotis, A. Douvas, P. Argitis, P. Normand, T. Gotszalk, M. Woszczyna, and N. Glezos, "Vertical devices of self-assembled hybrid organic/inorganic monolayers based on tungsten polyoxometalates," *Microelectron. Eng.*, vol. 85, no. 5–6, pp. 1399–1402, 2008.
- [83] S. Kim, D. Baek, J. Y. Kim, S. J. Choi, M. L. Seol, and Y. K. Choi, "A transistor-based biosensor for the extraction of physical properties from biomolecules," *Appl. Phys. Lett.*, vol. 101, no. 7, 2012.
- [84] K. K. Young, "Short-channel effect in fully depleted SOI MOSFETs," *Electron Devices, IEEE Trans.*, vol. 36, no. 2, pp. 2–5, 1989.
- [85] S. Khan, "QUANTUM MECHANICAL MODELING AND SIMULATION OF MONOLAYER WSe₂ CHANNEL FIELD EFFECT TRANSISTOR A thesis submitted in partial fulfillment of the requirements for the degree of Master of Science in Electrical and Electronic Engineering Saeed-Uz-Zaman Khan," Bangladesh University of Engineering and Technology, 2016.
- [86] "NanoTCAD ViDES." [Online]. Available: <http://vides.nanotcad.com/>. [Accessed: 01-Aug-2013].
- [87] "NanoTCAD ViDES." [Online]. Available: <http://vides.nanotcad.com/vides/>. [Accessed: 01-Sep-2015].

Appendix A

$$\eta_1 = \sqrt{\frac{4\varepsilon_{si}t_{si} + C_1t_{si}^2}{8C_1}}$$

$$\eta_2 = \sqrt{\frac{4\varepsilon_{si}t_{si} + C_2t_{si}^2}{8C_2}}$$

$$\eta_3 = \sqrt{\frac{4\varepsilon_{si}t_{si} + C_3t_{si}^2}{8C_3}}$$

$$\eta_4 = \sqrt{\frac{4\varepsilon_{si}t_{si} + C_4t_{si}^2}{8C_4}}$$

$$\sigma_1 = -\eta_1^2 \frac{qN_d}{\varepsilon_{si}} - (V_{gs} - V_{fb1})$$

$$\sigma_2 = -\eta_2^2 \frac{qN_d}{\varepsilon_{si}} - (V_{gs} - V_{fb2})$$

$$\sigma_3 = -\eta_3^2 \frac{qN_d}{\varepsilon_{si}} - (V_{gs} - V_{fb3})$$

$$\sigma_4 = -\eta_4^2 \frac{qN_d}{\varepsilon_{si}} - (V_{gs} - V_{fb4})$$

$$\psi_0 = V_{bi}$$

$$\psi_4 = V_{bi} + V_{ds}$$

$$n_1 = 2 \sinh\left(\frac{L_1}{\eta_1}\right)$$

$$n_1 = 2 \sinh\left(\frac{L_1}{\eta_1}\right)$$

$$n_2 = 2 \sinh\left(\frac{L_2}{\eta_2}\right)$$

$$n_3 = 2 \sinh\left(\frac{L_3}{\eta_3}\right)$$

$$n_4 = 2 \sinh\left(\frac{L_4}{\eta_4}\right)$$

$$o_1 = \exp\left(-\frac{L_1}{\eta_2}\right)$$

$$o_2 = \exp\left(-\frac{L_1 + L_2}{\eta_3}\right)$$

$$o_3 = \exp\left(-\frac{L_1 + L_2 + L_3}{\eta_4}\right)$$

$$q_1 = \exp\left(\frac{L_1}{\eta_1}\right)$$

$$q_2 = \exp\left(\frac{L_2}{\eta_2}\right)$$

$$q_3 = \exp\left(\frac{L_3}{\eta_3}\right)$$

$$q_4 = \exp\left(\frac{L_4}{\eta_4}\right)$$

$$x = \frac{1}{\eta_1}$$

$$y = \frac{1}{\eta_2}$$

$$z = \frac{1}{\eta_3}$$

$$z_1 = \frac{1}{\eta_4}$$

$$K_1 = q_1 + \frac{1}{q_1}$$

$$K_2 = q_2 + \frac{1}{q_2}$$

$$K_3 = q_3 + \frac{1}{q_3}$$

$$CC_0 = K_1 \frac{x}{n_1}$$

$$CC_1 = CC_0 q_1 \sigma_1 - CC_0 \sigma_1 - x q_1 \sigma_1$$

$$CC_2 = x q_1 - CC_0 q_1$$

$$CC_3 = K_2 \frac{y}{n_2}$$

$$CC_4 = CC_3 q_2 \sigma_2 - CC_3 \sigma_2 - y q_2 \sigma_2$$

$$CC_5 = y q_2 - CC_3 q_2$$

$$CC_{12} = K_3 \frac{z}{n_3}$$

$$CC_{13} = CC_{12} q_3 \sigma_3 - CC_{12} \sigma_3 - z q_3 \sigma_3$$

$$CC_{14} = z q_3 - CC_{12} q_3$$

$$CC_6 = 2 \frac{y}{n_2}$$

$$CC_7 = CC_6 q_2 \sigma_2 - CC_6 \sigma_2 - y \sigma_2$$

$$CC_8 = y - CC_6 q_2$$

$$CC_9 = 2 \frac{z}{n_3}$$

$$CC_{10} = CC_9 q_3 \sigma_3 - CC_9 \sigma_3 - z \sigma_3$$

$$CC_{11} = z - CC_9 q_3$$

$$CC_{15} = 2 \frac{z_1}{n_4}$$

$$CC_{16} = CC_{15} q_4 \sigma_4 - CC_{15} \sigma_4 - z_1 \sigma_4$$

$$CC_{17} = z_1 - CC_{15} q_4$$

$$A = \begin{pmatrix} CC_8 - CC_0 & CC_6 & \mathbf{0} \\ CC_5 & CC_3 - CC_{11} & -CC_9 \\ \mathbf{0} & CC_{14} & CC_{12} - CC_{17} \end{pmatrix}$$

$$B = \begin{pmatrix} \psi_0 CC_2 + CC_1 - CC_7 \\ CC_{10} - CC_4 \\ CC_{15} \psi_4 + CC_{16} - CC_{13} \end{pmatrix}$$

$$\begin{pmatrix} \psi_1 \\ \psi_2 \\ \psi_3 \end{pmatrix} = A^{-1} B$$

Appendix B

$$n = \sqrt{k_1}$$

$$p = \sqrt{k_1} L_{\text{bio}}$$

$$m = \sqrt{k_2}$$

$$r = \sqrt{k_2} L_2$$

$$\text{Den} = m(e^{2p} - 1)(e^{2r} - 1) + n(e^{2p} + 1)(e^{2r} - 1)$$

$$D_1 = V_s - \frac{A_1}{K_1}$$

$$D_2 = \frac{A_2}{K_2} - \frac{A_1}{K_1}$$

$$D_4 = V_d - \frac{A_2}{K_2}$$

$$A_{11} = n(e^{2r} - 1) - m(1 + e^{2r});$$

$$A_{12} = me^p(1 + e^{2r});$$

$$A_{14} = 2me^{p+r};$$

$$C_1 = \frac{(A_{11} * D_1 + A_{12} * D_2 + A_{14} * D_4)}{\text{Den}}$$

$$A_{21} = ne^{2p}(e^{2r} - 1) + me^{2p}(1 + e^{2r});$$

$$A_{22} = -A_{12};$$

$$A_{24} = -A_{14};$$

$$C_2 = \frac{(A_{21} * D_1 + A_{22} * D_2 + A_{24} * D_4)}{\text{Den}}$$

$$A_{31} = -2ne^p$$

$$A_{32} = n(1 + e^{2p})$$

$$A_{34} = me^r(e^{2p} - 1) + ne^r(1 + e^{2p})$$

$$C_3 = \frac{(A_{31} * D_1 + A_{32} * D_2 + A_{34} * D_4)}{\text{Den}}$$

$$A_{41} = 2ne^{p+2r};$$

$$A_{42} = -ne^{2r}(1 + e^{2p});$$

$$A_{44} = me^r(e^{2p} - 1) - ne^r(1 + e^{2p});$$

$$C_4 = \frac{(A_{41} * D_1 + A_{42} * D_2 + A_{44} * D_4)}{\text{Den}}$$

Appendix C

```
from NanoTCAD_ViDES import *
import sys
from module_TMD import *

rank = 0

# I create the grid
xg=nonuniformgrid(array([-9,1,0,0.05,9+2,1]))

FLAKE=TMD(70.0,"n");
FLAKE.me=0.51;
FLAKE.Egap=0.72;

acc=FLAKE.acc;
kF=2*pi/(3*sqrt(3)*acc);
kymax=4*pi/FLAKE.delta;
Nky=32.0;
dk=kymax/Nky;
FLAKE.kmax=pi/FLAKE.delta;
FLAKE.kmin=0;
FLAKE.dk=dk;

FLAKE.dE=0.01
grid=grid2D(xg,FLAKE.y,FLAKE.x,FLAKE.y);
savetxt("./datiout_DMFET/gridx.out",grid.gridx)
savetxt("./datiout_DMFET/gridy.out",grid.gridy)

# I take care of the solid
Oxide1=region("hex",grid.xmin,grid.xmax,grid.ymin,20)
Oxide1.eps=9;

Oxide2=region("hex",grid.xmin,grid.xmax,20,50)
```

```

Oxide2.eps=3.9;

Oxide3=region("hex",grid.xmin,grid.xmax,50,70)
Oxide3.eps=9;

TMDC=region("hex",0,2,grid.ymin,grid.ymax)
TMDC.eps=4.8;

top_gate=gate("hex",grid.xmax,grid.xmax,5.0,65.0);
bottom_gate=gate("hex",grid.xmin,grid.xmin,5.0,65.0);

p=interface2D(grid,Oxide1,Oxide2,Oxide3,TMDC,top_gate,bottom_gate);

fraction_source=0.001
fraction_drain=0.001
dope_reservoir(grid,p,FLAKE,fraction_source,array([0,2,grid.ymin,grid.ymax]));

Vgmin=-0.7;
Vgmax=0.3;
Vgstep=0.1;

Np=int(abs(Vgmin-Vgmax)/Vgstep)+1;
vg=zeros(Np);
current=zeros(Np);
p.underrel=0.1;

counter=0;
Vgs=Vgmin;
FLAKE.mu1=-0.0
FLAKE.mu2=-0.5

while (Vgs<=Vgmax):
    bottom_gate.Ef=-Vgs; set_gate(p,bottom_gate)
    top_gate.Ef=-Vgs; set_gate(p,top_gate)

```

```

p.normpoisson=1e-1;
p.normd=5e-3;
solve_self_consistent(grid,p,FLAKE);
vg[counter]=Vgs;
current[counter]=FLAKE.current();
# I save the output files
if (rank==0):
    string="./datiout_DMFET/Phi%s.out" %Vgs;
    savetxt(string,p.Phi);
    string="./datiout_DMFET/ncar%s.out" %Vgs;
    savetxt(string,p.free_charge);
    a=[FLAKE.E,FLAKE.T];
    string="./datiout_DMFET/T%s.out" %Vgs;
    savetxt(string,transpose(a));
    string="./datiout_DMFET/jayn%s.out" %Vgs;
    fp=open(string,"w");
    string2="%s" %current[counter];
    fp.write(string2);
    fp.close();
counter=counter+1;
Vgs=Vgs+Vgstep;

tempo=[vg,current]
savetxt("./datiout_DMFET/idvgs.out",transpose(tempo));

```